



**Single-Sided Noninvasive Inspection of
Multielement Sample Using Fan-Beam
Multiplexed Compton Scatter Tomography**

THESIS

Matthew A. Lange

AFIT/GAP/ENP/01J-01

**DEPARTMENT OF THE AIR FORCE
AIR UNIVERSITY**

AIR FORCE INSTITUTE OF TECHNOLOGY

Wright-Patterson Air Force Base, Ohio

APPROVED FOR PUBLIC RELEASE; DISTRIBUTION UNLIMITED.

Report Documentation Page

Report Date 01 Jun 2001	Report Type Final	Dates Covered (from... to) 01 Sep 1999 - 01 May 2001
Title and Subtitle Single-Sided Noninvasive Inspection of Multielement Sample Using Fan-Beam Multiplexed Compton Scatter Tomography	Contract Number	
	Grant Number	
	Program Element Number	
Author(s) Matthew A. Lange	Project Number	
	Task Number	
	Work Unit Number	
Performing Organization Name(s) and Address(es) Air Force Institute of Technology Graduate School of Engineering & Management (AFIT/EN) 2950 P Street, Building 640 WPAFB, OH 45433-7765	Performing Organization Report Number AFIT/GAP/ENP/01J-01	
Sponsoring/Monitoring Agency Name(s) and Address(es) AFRL/MLL 2230 10th Street, Room 123, WPAFB OH 45433 AFOSR/NA, 801 N. Randolph St., Arlington, VA 22203-1977	Sponsor/Monitor's Acronym(s)	
	Sponsor/Monitor's Report Number(s)	
Distribution/Availability Statement Approved for public release, distribution unlimited		
Supplementary Notes		

Abstract

As aircraft age, corrosion forms upon unobservable surfaces, particularly at the junction of the sheet aluminum and the steel rivets used to attach the sheets to the airframe, degrading the aircrafts airworthiness. Previous research developed a noninvasive technique for the evaluation of the material composition of aluminum surfaces, utilizing the information encoded in the energy spectra of Compton-scattered gamma emissions. The spectra are gathered by a six-element, high purity germanium detector array. A, first principles, deterministic computer code is used to reconstruct a two-dimensional map of the electron density of aluminum samples. Previous efforts, to image pure aluminum samples, suffered from: artifacts at sample boundaries, inaccurate determination of electron density values, and excessive sampling times of 41-111 hours. In this work images, of an oxidized aluminum sample including an iron insert meant to simulate a vertical two-dimensional slice through a steel rivet in an aluminum surface, have been reconstructed. Sample boundaries have been determined and included in reconstruction. Their inclusion in image reconstruction has reduced the artifacts on the edges of the sample and improved the accuracy of the values for electron density. An image, post-processing code has been implemented utilizing a priori knowledge of the electron densities of iron, aluminum, and air, to increase the accuracy of the density values determined by the reconstruction code. In addition, opening the field of view of the detector array has increased the throughput of the detectors, increasing peak measurements by approximately 900 counts per channel.

Subject Terms

Nondestructive Testing, Nondestructive Evaluation, Tomography, Computerized Tomography, Gamma Ray Scattering, Compton Scattering, Compton Scatter Imageing, Radiation Imaging, Radiological Imaging, Radition Measuring Instruments, Gamma Spectrometers

Report Classification

unclassified

Classification of this page

unclassified

Classification of Abstract

unclassified

Limitation of Abstract

UU

Number of Pages

94

The views expressed in this thesis are those of the author and do not reflect the official policy or position of the United States Air Force, Department of Defense, or the U. S. Government.

AFIT/GAP/ENP/01J-01

Single-Sided Noninvasive Inspection of Multielement Sample Using Fan-Beam
Multiplexed Compton Scatter Tomography

THESIS

Presented to the Faculty

Department of Engineering Physics

Graduate School of Engineering and Management

Air Force Institute of Technology

Air University

Air Education and Training Command

In Partial Fulfillment of the Requirements for the

Degree of Master of Science in Applied Physics

Matthew A. Lange, B.S.

May 2000

APPROVED FOR PUBLIC RELEASE; DISTRIBUTION UNLIMITED.

AFIT/GAP/ENP/01J-01

Single-Sided Noninvasive Inspection of Multielement Sample Using Fan-Beam
Multiplexed Compton Scatter Tomography

Matthew A. Lange, B.S.

Approved:

Larry W. Burggraf (Chairman)

date

Thomas N. Hangartner (Member)

date

James C. Petrosky (Member)

date

Acknowledgments

I would like to express my sincere appreciation to my faculty advisor, Dr. Larry Burggraf, for his guidance and support throughout the course of this thesis effort. The insight and experience was certainly appreciated. I would, also, like to thank Dr. Corneliu Costecu, his contribution to this work has been invaluable. David Gerts has made my life much easier by debugging FORTRAN code when needed. Thanks to Russ Hastings, Condie Inman, and Jan LeValley for their expertise in machining samples from poorly drawn plans, on the back of a napkin. Thanks to Brian Evans for his continued assistance in keeping the project moving. Thank you to my parents, without their support throughout all the avenues of my life I would be nothing.

Matt Lange

Table of Contents

ACKNOWLEDGMENTS	III
Table of Contents	iv
LIST OF FIGURES	VI
ABSTRACT	IX
CHAPTER 1: INTRODUCTION.....	1
1.1 RESEARCH OBJECTIVES.....	1
1.2 PHYSICS OF COMPTON SCATTERING.....	4
1.3 CENTRAL EQUATION FOR MCST.....	7
1.4 IMPROVEMENTS TO IMAGE RECONSTRUCTION	11
1.5 SUMMARY	12
CHAPTER 2: THEORY.....	14
2.1 INTRODUCTION.....	14
2.2 PWLS	15
2.3 DISCRETIZATION	19
CHAPTER 3: EQUIPMENT	22
3.1 FAN BEAM COLLIMATOR	22
3.2 HPGe DETECTOR ARRAY	23
3.3 DATA ACQUISITION.....	27
3.4 ¹⁰⁹ CD SOURCE	28
CHAPTER 4: RESULTS AND DISCUSSION.....	30
4.1 RIVET	30
4.1.1 Rivet Sample.....	31
4.1.2 Measurement Geometry	32
4.2 INITIAL RECONSTRUCTION	33
4.3 SAMPLE BOUNDARIES	39
4.3.1 Boundary Specification	39
4.3.2 Application of Boundaries to Rivet Sample	44
4.4 SMOOTHED MEASUREMENTS	51
4.5 WIDENED DETECTOR FIELD OF VIEW.....	55
4.5.1 Equipment Geometry.....	56
4.6 SECONDARY PEAK	61
CHAPTER 5: CONCLUSIONS.....	65
5.1 SUMMARY AND CONCLUSIONS	65
5.2 RECOMMENDATIONS	68
5.2.1 Experimental	68

5.2.2 Theoretical	69
APPENDIX A	71
WIDE FIELD OF VIEW	71
NARROW FIELD OF VIEW.....	74
WIDE COLLIMATION SETTINGS	76
NARROW COLLIMATION SETTINGS.....	77
APPENDIX B.....	78
INCLUSION OF TOP BOUNDARY	78
INCLUSION OF TOP AN BOTTOM BOUNDARIES	79
REFERENCES.....	80
VITA.....	82

List of Figures

FIGURE 1: SET OF ISOGONIC ARCS DEFINED BY POINT SOURCE AND DETECTOR POSITIONS (RIGHT) MESH OF ISOGONIC ARCS FROM MULTIPLE DETECTORS.(EVANS, 1999).....	5
FIGURE 2: ISOGONIC REGION DEFINED BY AN EXTENDED SOURCE AND DETECTOR.(EVANS, 1999).....	5
FIGURE 3: COMPARISON OF H AND AL COMPTON PROFILES (LEFT), AND IMPULSE APPROXIMATION ENERGY DISTRIBUTION OF 88keV PHOTONS SCATTERED THROUGH TWO DIFFERENT ANGLES.(EVANS, 1999).....	7
FIGURE 4: THE VALUE IN THE ZERO TH VOXELS IS INFLUENCED BY THE VALUES IN EACH OF ITS NEIGHBORING VOXELS ENCOURAGING NEIGHBORING VOXELS TO HAVE THE SAME ELECTRON DENSITIES.....	16
FIGURE 5: ALGORITHM OUTLINE FOR THE OUTER AND INNER ITERATIONS OF THE RECONSTRUCTION CODE (EVANS, 1999)	18
FIGURE 6: FLOW CHART SHOWING THE STEPS INVOLVED IN ATTAINING AN IMAGE WITH THE INCLUSION OF THE DISCRETIZATION STEP	21
FIGURE 7: NARROW COLLIMATION, (LEFT) VIEW OF DETECTOR ARRAY SIX BERYLLIUM WINDOWS AND (RIGHT) COLLIMATING TIN MASK AND THE DETECTOR HOUSING (EVANS, 1999)	24
FIGURE 8: TIN MASK WITH NARROW COLLIMATION (EVANS, 1999)	24
FIGURE 9: WIDE FIELD OF VIEW, (LEFT) NEW BERYLLIUM WINDOW ENCOMPASSING ALL SIX DETECTORS IN THE ARRAY AND (RIGHT) DETECTOR HOUSING WITHOUT THE TIN MASK	25
FIGURE 10: COMPARISON OF THE EFFICIENCY AS A FUNCTION OF ANGLE (DEGREES) BETWEEN THE NARROW FIELD OF VIEW (EVANS, 1999) AND THE WIDE FIELD OF VIEW GEOMETRIES FOR THE DETECTOR ARRAY USING 88keV PHOTONS.....	26
FIGURE 11: PULSE SHAPING ELECTRONICS FOR THE MCST SYSTEM (EVANS, 1999).....	27
FIGURE 12: SPECTRA FOR THE ¹⁰⁹ Cd SOURCE USED DURING SAMPLE MEASUREMENT, SHOWS CONTAMINATION PEAKS AN ORDER OF MAGNITUDE SMALLER THAN THE 88keV PEAK	29
FIGURE 13: SAMPLE SIMULATING ALUMINUM AIRFRAME SURFACE INCLUDING A STEEL RIVET AND CORROSION	31
FIGURE 14: SAMPLING GEOMETRY USED FOR THE RIVET SAMPLE	32
FIGURE 15: SECOND POSITION FOR THE RIVET SAMPLE. ASSUMING SYMMETRIC RESULTS OF THE MEASUREMENTS MADE IN THE ORIGINAL POSITION YIELDS THE SPECTRA FOR THIS POSITION	33
FIGURE 16: 2-DIMENSIONAL PROJECTION OF ELECTRON DENSITY MAP, X AND Y-AXES MAP VOXEL COORDINATE WHILE SHADE INDICATES DENSITY VALUE.	34
FIGURE 17: IMAGE OF THE RIVET SAMPLE, PERFECT DENSITY VALUES. HEIGHT (LEFT AXIS) IS THE ELECTRON DENSITY, FOR AL = 2.7, FE = 7.3, AIR = 0.0, SHADES SHOW TRANSITION FROM INTEGER NUMBERS.....	34

FIGURE 18: 2-DIMENSIONAL PROJECTION OF ELECTRON DENSITY MAP USING SIMULATED SPECTRA, X AND Y-AXES MAP VOXEL COORDINATE WHILE SHADE INDICATES DENSITY VALUE.	35
FIGURE 19: IMAGE RECONSTRUCTED FROM SIMULATED DATA, NO ASSUMPTIONS ABOUT BOUNDARIES, HEIGHT (LEFT AXIS) IS THE ELECTRON DENSITY, FOR AL = 2.7, Fe = 7.3, AIR = 0.0, SHADES SHOW TRANSITION FROM INTEGER NUMBERS.	36
FIGURE 20: COMPARISON OF SIMULATED TO MEASURED SPECTRA, COUNTS (ARB. UNIT) VS. ENERGY IN KEV	37
FIGURE 21: 2D PROJECTION OF ELECTRON DENSITY MAP FROM MEASURED DATA, NO ASSUMPTIONS ABOUT BOUNDARIES, X AND Y-AXES MAP VOXEL COORDINATE WHILE SHADE INDICATES DENSITY VALUE.	38
FIGURE 22: IMAGES FROM MEASURED DATA, NO ASSUMPTIONS ABOUT BOUNDARIES, HEIGHT (LEFT AXIS) IS THE ELECTRON DENSITY, FOR AL = 2.7, Fe = 7.3, AIR = 0.0, SHADES SHOW TRANSITION FROM INTEGER NUMBERS.	38
FIGURE 23: NUMBER OF COUNTS FROM 55 TO 90KEV OVER 14,000 SECS, AS THE THICKNESS OF AL VARIES FROM 4 TO 16MM.....	40
FIGURE 24: ILLUSTRATION OF THE COLLIMATION PARAMETERS REQUIRED FOR THE EXECUTION OF SCATGRAM(COSTESCU)	43
FIGURE 25: 2D PROJECTION OF ELECTRON DENSITY MAP (TOP) PLOT OF ACTUAL SAMPLE AND (BOTTOM) RECONSTRUCTION FROM MEASURED DATA, ASSUMING TOP BOUNDARY IS KNOWN, X AND Y-AXES MAP VOXEL COORDINATE WHILE SHADE INDICATES DENSITY VALUE.	44
FIGURE 26: IMAGE OF RIVET RECONSTRUCTED ASSUMING THE TOP BOUNDARY IS KNOWN, HEIGHT (LEFT AXIS) IS THE ELECTRON DENSITY, FOR AL = 2.7, Fe = 7.3, AIR = 0.0, SHADES SHOW TRANSITION FROM INTEGER NUMBERS.	45
FIGURE 27: 2D PROJECTION OF ELECTRON DENSITY MAP (TOP) PLOT OF ACTUAL SAMPLE AND (BOTTOM) RECONSTRUCTION FROM MEASURED DATA, ASSUMING TOP AND BOTTOM BOUNDARY IS KNOWN, X AND Y-AXES MAP VOXEL COORDINATE WHILE SHADE INDICATES DENSITY VALUE	46
FIGURE 28: IMAGE OF RIVET INCLUDING TOP AND BOTTOM BOUNDARIES, HEIGHT (LEFT AXIS) IS THE ELECTRON DENSITY, FOR AL = 2.7, Fe = 7.3, AIR = 0.0, SHADES SHOW TRANSITION FROM INTEGER NUMBERS.....	47
FIGURE 29: 2D PROJECTION OF ELECTRON DENSITY MAP (TOP) PLOT OF ACTUAL SAMPLE AND (BOTTOM) RECONSTRUCTION FROM SIMULATED DATA, ASSUMING TOP AND BOTTOM BOUNDARY IS KNOWN, X AND Y-AXES MAP VOXEL COORDINATE WHILE SHADE INDICATES DENSITY VALUE	48
FIGURE 30: RECONSTRUCTION OF RIVET FROM SIMULATED DATA, ASSUMING BOTH TOP AND BOTTOM BOUNDARIES ARE KNOWN, HEIGHT (LEFT AXIS) IS THE ELECTRON DENSITY, FOR AL = 2.7, Fe = 7.3, AIR = 0.0, SHADES SHOW TRANSITION FROM INTEGER NUMBERS.	49
FIGURE 31: (TOP) ILLUMINATED VOXELS ARE WHITE WHILE VOXELS NOT IN INSPECTION REGION ARE BLACK, 2D PROJECTION OF ELECTRON DENSITY MAP (MIDDLE) PLOT OF ACTUAL SAMPLE AND (BOTTOM) RECONSTRUCTION FROM MEASURED DATA,	

ASSUMING TOP AND BOTTOM BOUNDARY IS KNOWN, X AND Y-AXES MAP VOXEL COORDINATE WHILE SHADE INDICATES DENSITY VALUE.....	50
FIGURE 32: IMAGE OF RIVET FROM SIMULATED DATA, ASSUMING TOP, BOTTOM AND THE LEFT AND RIGHT BOUNDARIES ARE KNOWN, HEIGHT (LEFT AXIS) IS THE ELECTRON DENSITY, FOR $Al = 2.7$, $Fe = 7.3$, $Air = 0.0$, SHADES SHOW TRANSITION FROM INTEGER NUMBERS.	51
FIGURE 33: COMPARISON OF SMOOTHED MEASUREMENTS TO THE SIMULATED SPECTRA, COUNTS (ARB. UNITS) VS. ENERGY (KEV)	53
FIGURE 34: REDUCTION OF BETA TO ALLOW PWLS TO CONVERGE TO LOWER DENSITIES WHERE APPROPRIATE AND DESCRETIZATION CODE INCLUDING FIXING THE VOXELS TO DISCRETE DENSITIES KNOWN TO EXIST IN THE SAMPLE AND ALLOW DISCONTINUOUS CHANGES IN DENSITY	54
FIGURE 35: (TOP) GEOMETRY OF THE DETECTOR ARRAY WHEN THE WIDE FIELD OF VIEW IS USED AND (BOTTOM) THE DETECTOR GEOMETRY WHEN THE NARROW FIELD OF VIEW PLATE IS IN FRONT OF THE DETECTOR ARRAY	56
FIGURE 36: THE MEASURED AND SIMULATED SPECTRA FOR WIDE AND NARROW FIELD OF VIEW FOR DETECTOR 6, COUNTS (ARB. UNITS) VS. ENERGY (KEV).....	58
FIGURE 37: THE MEASURED AND SIMULATED SPECTRA FOR WIDE AND NARROW FIELD OF VIEW FOR DETECTOR 5, COUNTS (ARB. UNITS) VS. ENERGY (KEV).....	59
FIGURE 38: 2D PROJECTION OF ELECTRON DENSITY MAP (TOP) PLOT OF ACTUAL SAMPLE AND (BOTTOM) RECONSTRUCTION FROM SIMULATED DATA, ASSUMING ALL BOUNDARIES ARE KNOWN, USING WIDE FOV, X AND Y-AXES MAP VOXEL COORDINATE WHILE SHADE INDICATES DENSITY VALUE.....	60
FIGURE 39: COUNTS VS. ENERGY (KEV), FOUR SPECTRA MEASURED BY DETECTOR 6, RESULTING FROM 4, 8, 12, AND 16MM THICK SAMPLES OF AL PLACED IN FRONT OF THE DETECTOR ARRAY	62
FIGURE 40: COUNTS UNDER PEAKS SHOWING SAME PROPORTIONS FROM SINGLY SCATTERED PEAK AND THE SECONDARY PEAK.....	63
FIGURE 41: PEAK LOCATION AS A FUNCTION OF THE X POSITION OF THE DETECTORS.....	64

Abstract

As aircraft age, corrosion forms upon unobservable surfaces, particularly at the junction of the sheet aluminum and the steel rivets used to attach the sheets to the airframe, degrading the aircraft's airworthiness. Previous research developed a noninvasive technique for the evaluation of the material composition of aluminum surfaces, utilizing the information encoded in the energy spectra of Compton-scattered gamma emissions. The spectra are gathered by a six-element, high purity germanium detector array. A, first principles, deterministic computer code is used to reconstruct a two-dimensional map of the electron density of aluminum samples. Previous efforts to image pure aluminum samples suffered from: artifacts at sample boundaries, inaccurate determination of electron density values, and excessive sampling times. In this work images, of an oxidized aluminum sample including an iron insert meant to simulate a vertical two-dimensional slice through a steel rivet in an aluminum surface, have been reconstructed. Sample boundaries have been determined, and included in reconstruction. Their inclusion in image reconstruction has reduced the artifacts on the edges of the sample and improved the accuracy of the values for electron density. An image, post-processing code has been implemented utilizing *a priori* knowledge of the electron densities of iron, aluminum, and air, to increase the accuracy of the density values determined by the reconstruction code. In addition, opening the field of view of the detector array has increased the

throughput of the detectors, increasing peak measurements by approximately 900 counts per channel.

Single-Sided Noninvasive Inspection of Multielement Sample Using Fan-Beam Multiplexed Compton Scatter Tomography

Chapter 1: Introduction

The United States Air Force is interested in the development of a device able to nondestructively evaluate the structural integrity of an aircraft. Currently, the solution is dismantling of aircraft to allow direct inspection of hidden surfaces. This method is costly. A device able to rapidly detect structural faults, such as corrosion, in the unobservable regions of the airframe by scanning the aircrafts surface could make significant financial savings for the US Air Force.

1.1 Research Objectives

The overall vision of this research is the realization of an imaging system capable of creating radiographic images of the electron density from the information encoded in the energy spectra of gamma rays backscattered from an aircraft. A method to accomplish this has been developed by Brian Evans (Evans, 1999). Evans has developed a first-principals, deterministic code utilizing the information encoded in the energy spectra of Compton scattered photons to create two-dimensional electron density mappings of thin aluminum samples. His work also included the design and testing of a prototype

multiplexed Compton scatter tomograph (MCST) imaging system consisting of a 6-element detector array and associated electronics. (Evans, 1999)

The existing method has some shortcomings. The images realized during previous research were limited to providing information about the change in density from one area of the sample to the other; however, the exact density of the sample in any particular region of space was not accurately represented. The time required to attain spectra with a signal to noise ratio large enough to facilitate image reconstruction, 41-111 hours, is too large for a practical system. Also, the image reconstruction algorithm includes a smoothing term, which causes blurring of sample boundaries resulting in an overall degradation of the image. Finally, the code has yet to be used in the reconstruction of more complex samples characteristic of the types of material combinations encountered in aircraft, namely aluminum oxide in the presence of a steel rivet.

The goal of this research is to expand and improve the capabilities of the MCST system developed previously. Specifically, defining the boundaries of the sample allows the image reconstruction algorithm to attain more representative electron density values. Opening the field of view of the detector array increases the signal throughput, increasing the signal to noise ratio of the recorded energy spectra. Application of the technique to the realistic geometry of the rivet expands the abilities of the method.

Incorporating the location of the boundaries of the inspection region in the image reconstruction significantly affects image fidelity. Included in the image

reconstruction algorithm is a smoothing term, which encourages neighboring volume elements (voxels) to have the same densities. When a voxel is located on an edge of the sample, the neighboring voxels are air. Therefore, the smoothing term encourages voxels along the samples edge to take on the electron density of air incorrectly placing areas of void within the bulk aluminum. Including the location of the boundaries of the inspection region results in more accurate determination of the electron density measurements and reduces the number of artifacts present in the images.

The field of view of all of the detectors in the array has been opened in an effort to increase the throughput of the detectors. This has been accomplished by redesigning the beryllium window of the cryostat assembly. The current design has one large aperture in front of the entire array of detectors allowing each detector to observe a larger region than the original design allowed. This change has increased the throughput of each detector, increasing the peak counts by approximately 900 counts per channel, allowing for better signal to noise ratio for an equivalent counting period.

The final element of this work is the implementation of this device to interrogate a two-dimensional aluminum sample including a steel rivet. This geometry is more complicated than previous examples, and it is postulated that the inclusion of a higher atomic number (Z) iron material will cause a loss in signal due to enhanced gamma absorption.

1.2 Physics of Compton Scattering

The Multiplexed Compton Scatter Tomograph (MCST) interrogates multiple volume elements or voxels simultaneously. The intensity of the radiation scattering from any given voxel is directly proportional to the electron density in that voxel. The scattered radiation is gathered by a 6-element array of high-purity germanium (HPGe) detectors. The spectra, collected by the detector array, are used to construct an electron density mapping of the sample. Decoding the density information from the measured spectra requires a precise knowledge of the photon energy of the incident flux. Therefore, a radionuclide, emitting a single-energy gamma, must be utilized rather than an x-ray tube, which provides broadband emissions. The underlying principle of this system is the relationship between the energy E' of a photon scattered from a stationary electron and its' initial energy E_0 .

$$E' = \frac{E_0}{1 + \frac{E_0}{m_0 c^2} (1 - \cos \theta)} \quad (1)$$

Where m_0 is the rest mass of an electron, c is the speed of light, and θ is the scattering angle of the photon. Given the initial and final paths of the photon, the information concerning the location of the scattering event may be derived from the angle θ . The possible scattering positions of any E_0, E' pair is represented

by an isogonic-arc. The isogonic-arcs originating from a range of detected energies and a number of detectors is illustrated in figure 1.

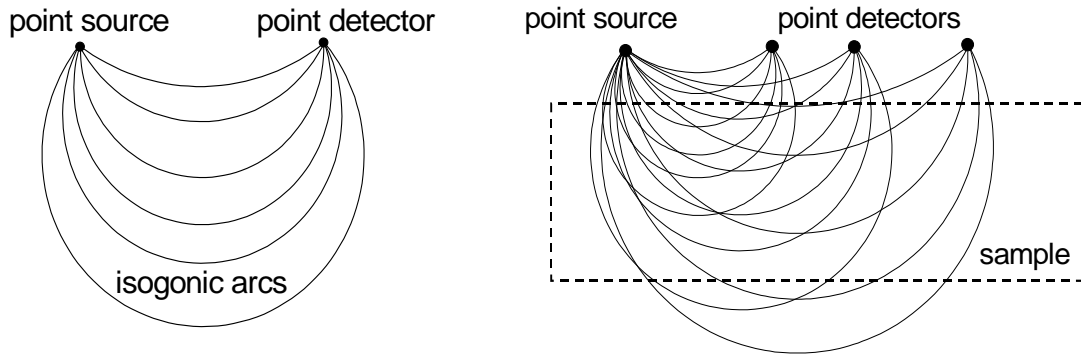


Figure 1: Set of isogonic arcs defined by point source and detector positions (right) mesh of isogonic arcs from multiple detectors.(Evans, 1999)

The sources and detectors used as examples thus far have been theoretical points. Giving these points physical dimensions will cause the isogonic arcs to become isogonic regions.(Evans, 1999)

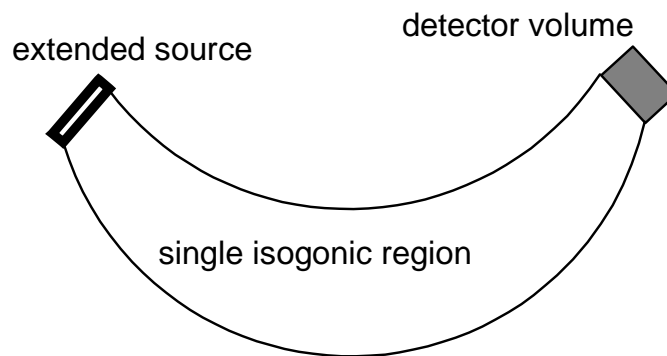


Figure 2: Isogonic region defined by an extended source and detector.(Evans, 1999)

The Klein-Nishina relation provides the differential cross-section for Compton scattering at angle θ per unit solid angle $d\Omega$. It is given in equation 2 per free electron for unpolarized radiation.

$$\left(\frac{d\sigma}{d\Omega}\right) = \frac{1}{2}r_0^2 \left(\frac{E'}{E_0}\right)^2 \left(\frac{E'}{E_0} + \frac{E_0}{E'} - \sin^2 \theta\right) \quad (2)$$

Both the Compton equation and the Klein-Nishina relationship are based on the assumption that the electron in the interaction is stationary. In general, electrons are not stationary and blur the one-to-one relationship between angle of scatter and E' . The result is a distribution of resultant E' values for any E_0 , θ combination. This effect, called Doppler broadening, is significant at energies below 200keV.

The impulse approximation is invoked to describe Doppler broadening. The differential cross-section per differential energy dE' and differential solid angle $d\Omega$ is (Cooper, 1997; Ribberfors, 1982)

$$\frac{d^2\sigma_s}{d\Omega dE'} = \frac{m_0 r_0}{2\sqrt{E_0^2 + E'^2 - 2E_0 E' \cos \theta}} \cdot \left(\frac{E'}{E_0}\right) \left(\frac{E'}{E_0} + \frac{E_0}{E'} - \sin^2 \theta\right) \cdot J(p_z) \quad (3)$$

$J(p_z)$ is the Compton profile of the scattering atom (Biggs, 1975). The impulse approximation for scattering of 88keV gammas from aluminum at two different

angles is shown in figure 3. The broadening is a non-Gaussian function of the scattering angle, and the effects of Doppler Broadening are observable using detectors with resolution of several hundred keV (Evans, 1999).

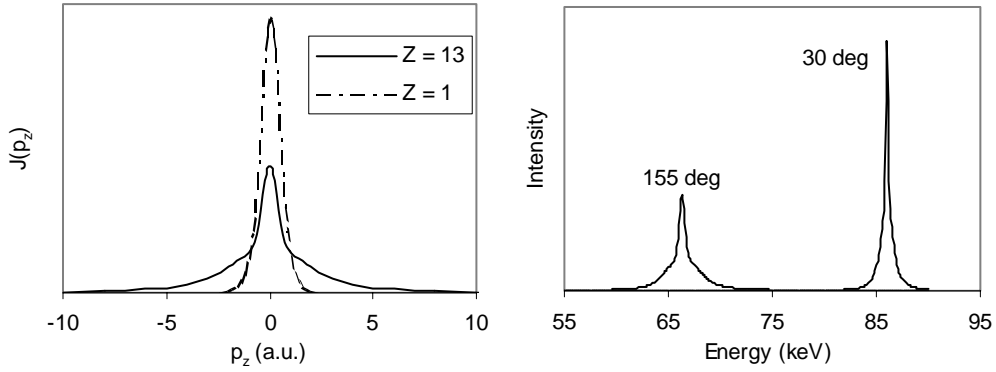


Figure 3: Comparison of H and Al Compton Profiles (left), and impulse approximation energy distribution of 88keV photons scattered through two different angles.(Evans, 1999)

1.3 Central equation for MCST

As described by Arendtsz, the central exercise of MCST is embodied in the system equation (Arendtsz, 1995).

$$\vec{\Psi} = \vec{A}(\vec{\rho}) \cdot \vec{\rho} \quad (4)$$

Where $\vec{\Psi}$ represents the set of multiple energy spectra sorted into a vector, $\vec{\rho}$ represents the set of voxel densities sorted into a vector, and $\vec{A}(\vec{\rho})$ represents a

mapping of the voxel densities to the spectra measurements. $\vec{A}(\vec{\rho})$ is expressed as an implicit function of $\vec{\rho}$ because the attenuation of radiation incident on and scattered from any particular voxel is dependant in a nonlinear way on the densities of many other voxels.

Image reconstruction involves estimating $\vec{\rho}$ given $\vec{\Psi}$, and cannot proceed without first building the system model $\vec{A}(\vec{\rho})$. The objective is to describe how the density in any voxel manifests itself in the set of energy measurements. First principles, deterministic computer codes were developed by Evans to construct this system model. The codes are complex algorithms that incorporate, for example, many system geometry parameters, detector efficiency and resolution, and Doppler broadening of scattered photons. Realistic modeling of source and detectors as finite-sized features means that for every voxel the code integrates across possible incident photon paths from the source and across possible scattered photon paths to the detector. The contribution of each possible scattering path is projected onto $\vec{\Psi}$. Each projection is assigned a probability and distributed in energy according to the impulse approximation, convolved with an energy-variant function to account for detector resolution, and corrected for detector efficiency as a function of energy and of the angle of photon incidence. An objective of the first principles approach was to produce a high-fidelity model that minimized reliance on experimentally measured detector response functions. (Evans, 1999)

The deterministic $\vec{A}(\vec{\rho})$ model was validated by comparison with MCNP simulations and verified experimentally by comparison with the point response collected from small-diameter aluminum scattering targets. (Evans, 1999)

The nature of the MCST problem requires some special considerations during image reconstruction. The dependence of the system matrix upon the density vector in equation (4) suggests that solving for $\vec{\rho}$ by direct inversion is not possible, calling for an iterative technique beginning with an initial guess for $\vec{\rho}$. The approach taken by Evans et al was a two-level iteration procedure in which the values of $\vec{\rho}^{k+1}$ were converged during the “inner” iteration based on a fixed system matrix $\vec{A}(\vec{\rho}^k)$ constructed from the last converged set of solution values $\vec{\rho}^k$. Once $\vec{\rho}^{k+1}$ converges, the “outer” iteration step consists of updating the nonlinear $\vec{\rho}$ dependencies in the system matrix, (i.e. computing $\vec{A}(\vec{\rho}^{k+1})$). The inner iteration proceeds again to converge new solution values $\vec{\rho}^{k+2}$ based on a fixed $\vec{A}(\vec{\rho}^{k+1})$. The reconstruction is considered complete when the outer iteration converges to some established criteria, (i.e. when $\vec{\rho}^{k+1} \approx \vec{\rho}^k$). (Evans, 1999)

The MCST system matrix is so poorly conditioned, however, that the solution is highly sensitive to random noise in the signal as well as small errors in the accuracy of the system model. Without some kind of regularization, the solution that best matches noisy data is highly oscillatory and does not represent

a reasonable approximation of sample densities. Therefore, the inner iteration algorithm is a weighted least squares fit to the data with the inclusion of a penalization term. The weighting term is inversely related to the variance in the measurements regularizing the noise in the spectra while the penalization term corrects for the effects of the ill-conditioned matrix by encouraging neighboring voxels to assume the same values. The reconstruction algorithm is discussed in greater detail in Chapter 2.

Photons that scatter more than once in the sample and are subsequently registered in a detector are signal contaminants because they do not carry the relationship between energy and scattering angle that localizes singly scattered events. Furthermore, it is not possible to discriminate between these photons on an event-by-event basis. Monte Carlo simulation revealed that the multiple scatter contribution to the signal is relatively insensitive to the geometry of the sample, although the intensity of the contribution is proportional to the volume of the sample under interrogation (Gerts, 1999). The essentially flat and featureless spectrum of multiply-scattered photons extends below that of the single-scatter contribution. These characteristics made it possible to develop an *ad hoc* estimate of the signals multiple scatter component on the basis of the counts in the lower-energy bins. While these considerations are not rigorously derived, the multiple scatter estimates improve image quality.

1.4 Improvements to Image Reconstruction

The method above has been applied to a number of aluminum samples during the work of Evans. The resulting images contain artifacts along the edges of the samples due to the smoothing of the air surrounding the sample into the sample volume. Furthermore, the electron densities attained by the algorithm do not approach the values present in the sample, even though they do reflect the variations in electron density within the sample. Sample boundaries and a post processing discretization process are incorporated into the reconstruction mechanism to decrease the divergence of the images from the physical system.

The inclusion of sample boundaries allows voxel density values to make an immediate transition from the density of the sample to that of air without the smooth transition caused by sample smoothing. It is argued that the top surface of the sample may be determined by a positioning system and the left and right boundaries of the inspection region are determined by the geometry of the gamma source and collimation. Additionally, it has been shown in this work that the surface opposite the detector array may be determined from the summed intensity of the detectors in the array. The specifics of these adjustments and their effects upon image reconstruction are discussed in chapter 4.

The need for a regularizing term within the reconstruction code, to diminish the effects of the poorly conditioned system matrix, is acute; however, the effect of this term does not permit the reconstruction of step discontinuities in the sample and encourages the algorithm to realize voxel densities which are not

representative of sample materials. The inclusion of a post-processing step fixes the voxel densities to values determined by the user, *a priori* to image reconstruction. This step forces the voxels to attain values representative of the sample densities and establishes step discontinuities in the sample. This technique will be discussed further in chapter 2.

1.5 Summary

Multiplexed Compton scattering tomography (MCST) is an imaging technique, which reconstructs the electron densities of a sample. The measurements may be performed on samples where only one side is available for inspection because it utilizes scattered signals rather than transmitted signals.

Compton scattering is the interaction of a photon with an electron resulting in alteration of the photon trajectory and energy. The detectors have a relatively wide field of view allowing them to examine a plane of material rather than a spot-by-spot evaluation. MCST multiplexes in energy and detectors allowing the evaluation of multiple voxels simultaneously.

To ensure a significant number of photons scatter within the aluminum samples, photons in the energy range of are used. In this energy regime the photons are subject to Doppler broadening complicating the relationship between scattering direction and photon energy depicted in the Compton equation.

The MCST image reconstruction algorithm suffers from a poorly conditioned system matrix, requiring care be taken during image reconstruction. Although accurate representation of the changes in electron density from region to region is constructed relatively well, images do not accurately reproduce the electron densities in the sample. The sampling duration is unrealistic for real world applications. The inclusion of other materials in the samples, such as steel, exhibits the MCST system ability to evaluate a larger variety of sample geometries.

Chapter 2 describes the deterministic MCST code developed by Evans. The theory of the added discretization method, adapted from Sauer and Bouman (1993), will also be discussed.

Chapter 3 describes the components of the MCST system. The system includes an array of HPGe detectors, a ^{109}Cd photon source, collimation, and the associated electronics.

Chapter 4 reports the effects upon resultant images as boundaries are determined and the discretization method is implemented. Also included are spectral features previously unobserved and their probable causes.

Chapter 5 gives conclusions and suggestions for further work.

Chapter 2: Theory

2.1 Introduction

Reconstructed images utilizing the information contained in the spectra of singly, Compton scattered photons are two-dimensional plots of the samples electron density. The problem is the inverse of the MCST system equation.

$$\vec{\Psi} = \vec{A}(\vec{\rho}) \cdot \vec{\rho} \quad (5)$$

The reconstruction algorithm utilizes the measured spectra, $\vec{\Psi}$, to obtain the corresponding values of $\vec{\rho}$ subject to the system matrix $\vec{A}(\vec{\rho})$. The system matrix is typically poorly conditioned and the measured spectra are noisy. These conditions make the solution to this problem difficult to obtain.

The method chosen for this task is the Penalized Weighted Least Squares (PWLS) algorithm developed by Fessler (1994) and adapted to the MCST system by Evans (1999). In order to improve the condition of the system matrix and dissuade the effects of smoothing, a discretization method developed by Sauer (1993) has been applied in this work. The discretization algorithm reduces the solution set using *a priori* knowledge of the sample.

2.2 PWLS

The PWLS is an element-by-element updating method seeking to minimize the objective function equation 6. The use of pure likelihood-based methods is impossible due to the noise associated with the measured spectra. Therefore, a weighted least squares algorithm is needed

$$\frac{1}{2}(\hat{p} - \mathbf{A}f)' \mathbf{D}^{-1} (\hat{p} - \mathbf{A}f) \quad (6)$$

Where $'$ denotes transpose, f are the density elements of the image, \mathbf{A} is the system matrix, \hat{p} is the vector of measured spectra, and \mathbf{D} is the diagonal matrix of the inverse of the variances. The diagonal matrix provides weighting terms, which are large for measurements with high signal to noise while small for elements with contributions having smaller signal to noise. The intent of this term is to encourage the system solution to be driven by measurements having higher level of accuracy and thereby decreasing the effect of the ever-present noise. The disadvantage of this weighting approach is that subtle spectral features from deeper in the sample are lost. Assuming Poisson statistics, the values of the weighting matrix are:

$$D_{nn} = \sigma_{g(n)-b(n)}^2 \quad (7)$$

The conditioning of the system matrix allows the solutions to sporadically vary in value from voxel to voxel. This manifests itself, for instance, by the inclusion of a voxel of air within the bulk of the aluminum sample. The development of oxide within the bulk of the material is unrealistic based on current scientific understanding of oxidation mechanisms and observations of corrosion at interfaces; therefore, a smoothing or penalizing term has also been included in the algorithm encouraging neighboring voxels to have the same values. The penalization function implemented is a median smoothing function and takes the form

$$\beta R(f) = \beta \frac{1}{2} \sum_{m=1}^{N_x N_z} \sum_{n \in N_m} w_{mn} \frac{1}{2} (f(n) - f(m))^2 \quad (8)$$

β is a weighting term that enables the amount of smoothing to be determined by the user, N_x and N_z are the number of voxels in the x and z directions of the 2D sample space respectively, and N_m are the eight neighboring voxels of element n. The weighting function is much clearer when pictured below in figure 4.

$1/\sqrt{2}$	1	$1/\sqrt{2}$
1	0	1
$1/\sqrt{2}$	1	$1/\sqrt{2}$

Figure 4: The value in the zeroth voxels is influenced by the values in each of its neighboring voxels encouraging neighboring voxels to have the same electron densities

As may be seen above, the penalization function weights adjacent voxels by 1 and diagonal neighbors by $1/\sqrt{2}$. The smoothing term is implemented in the reconstruction algorithm as

$$\frac{1}{2}(\hat{p} - \mathbf{A}f)' \mathbf{D}^{-1}(\hat{p} - \mathbf{A}f) + \beta R(f) \quad (9)$$

An over-relaxation technique is used, by Fessler and implemented in our method to minimize the objective function of the equation

$$f'^{k+1}(n) = \varpi \frac{\mathbf{A}_n \mathbf{D}^{-1} r + s(n) f'^k(n) + \beta R(f'^k)}{s(n)} + (1 - \varpi) f'^{old}(n) \quad (10)$$

Where ϖ is a weighting term and r is the latest residual

$$r = \hat{p} - \mathbf{A}f \quad (11)$$

and $s(n)$ denotes the n^{th} column of \mathbf{A}

$$s(n) = \mathbf{A}_n^T \mathbf{D}^{-1} \mathbf{A}_n \quad (12)$$

The A matrix is a function of the density values for which the algorithm is solving. This non-linearity is caused by attenuation of the signal into and out of the sample and requires the implementation of the iterative procedure discussed in chapter 1 to obtain a solution for the system matrix. The algorithm uses an initial guess containing no corrosion for the voxel values. Using these density values a temporary system matrix is determined and used to solve for an initial guess of the density values in the sample. After a new set of voxel densities are produced using the PWLS algorithm, the system matrix must be updated and PWLS repeated. This process is repeated as many times as the user requires, usually until a desired residual value is attained. The process is as pictured in figure 5

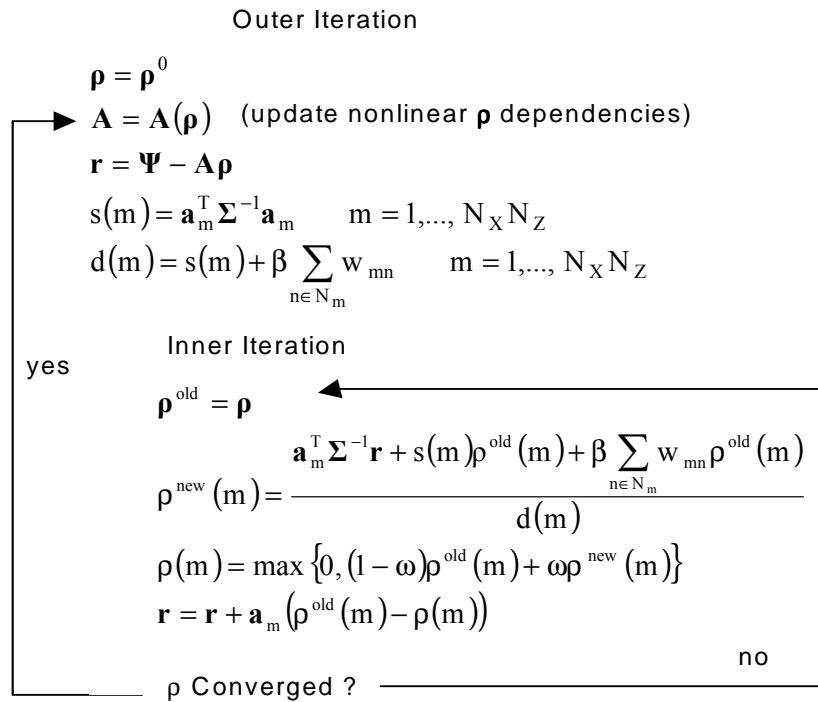


Figure 5: Algorithm outline for the outer and inner iterations of the reconstruction code (Evans, 1999)

In an attempt to reduce the amount of smoothing caused by the PWLS algorithm and simultaneously improve the conditioning of the system matrix, by reducing the size of the solution space, a discretization method has been added to the reconstruction algorithm.

2.3 Discretization

To improve the MCST reconstruction code, it is necessary for the resultant images to have electron densities representative of those existent in the samples and to reconstruct distinct boundaries between materials. This is important when phantoms contain boundaries that are step functions from one material to the next. The current reconstruction algorithm, using the PWLS reconstruction method, cannot realize these step functions due to the smoothing/penalization term. In response to this, a post-processing step has been incorporated into the code, which allows the images to have step discontinuities in density. (Shown in figure 6) The algorithm is implemented from the method derived by Bouman and Sauer (Sauer, 1993).

$$\hat{f}_j = \arg \max_{x \in O} \left\{ \theta_1 (x - f_j) - \frac{\theta_2}{2} (x - f_j)^2 - \gamma \left(v_1 (x, f_{\partial j}) + \frac{v_2 (x, f_{\partial j})}{\sqrt{2}} \right) \right\} \quad (13)$$

where O is the set of feasible densities for a pixel, $v_1(x, f_{\partial j})$ counts the number of horizontal and vertical neighbors of f_j which do not have the density x , and $v_2(x, f_{\partial j})$ counts the number of diagonal neighbors of f_j which do not have the density x . The values of θ_1 and θ_2 are defined as:

$$\theta_1 = \mathbf{A}_{*i}^t \mathbf{D} e \quad (14)$$

$$\theta_2 = \mathbf{A}_{*i}^t \mathbf{D} \mathbf{A}_{*i}, \quad (15)$$

where \mathbf{A}_{*i}^t is the i^{th} column of \mathbf{A} , e is the projection error, and \mathbf{D} is the diagonal matrix of the inverse of the variances. The possible values of the density are dictated by *a priori* knowledge of the sample.

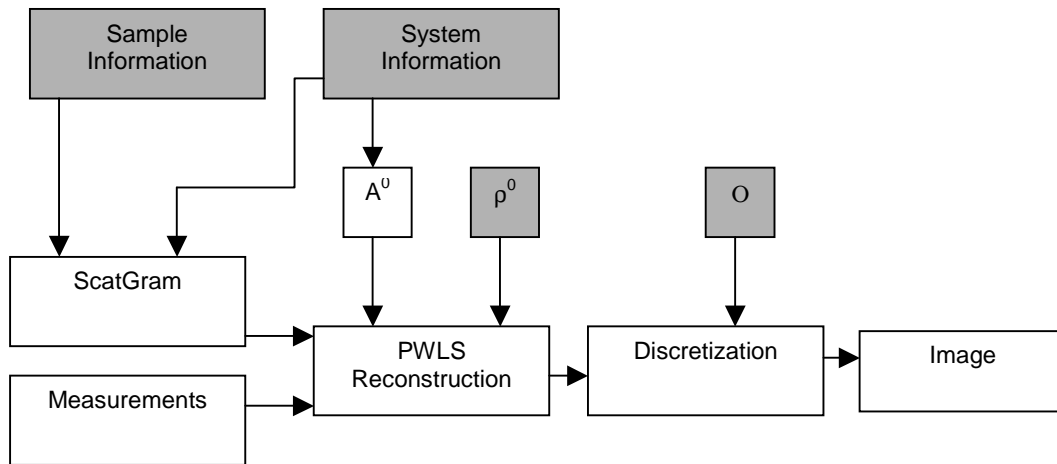


Figure 6: Flow chart showing the steps involved in attaining an image with the inclusion of the discretization step

By restricting the allowed values for the densities of the pixels, the solution space has been reduced in size thereby improving the condition of the solution matrix. Also, this method will allow the images to reflect the step discontinuities between one sample material and another, obvious at the boundary between the steel rivet and the aluminum frame.

Chapter 3: Equipment

The main components of the MCST demonstration system are the ^{109}Cd radio nuclide gamma source, the collimator, the six detector array, the pulse shaping electronics, and the data acquisition system. The fan beam collimator, system electronics, and radiation shielding remain unchanged from those experimental elements used by Evans and will not be explained in detail. The ^{109}Cd radio nuclide and the high purity germanium (HPGe) detector have been altered and will be discussed in detail.

3.1 Fan Beam Collimator

The fan beam collimator limits the field of view (FOV) of the source and the detector array to a single plane. The current reconstruction algorithm is based on a two-dimensional (2D) system, requiring that only a 2D region be illuminated by the source. Furthermore, the collimator reduces the contribution from multiple scatters by limiting the detector field of view to the plane of interest. An important material property of the collimator is that it has been constructed from tin. Tin is used instead of lead because the photon peak used by the simulations is the 88keV gamma peak originating from the ^{109}Cd source. Lead has an x-ray peak at 88.03keV, which may be excited by background radiations.

Thus, lead emits photons at this energy subsequently distributing the gamma source throughout a large area of space corrupting the measurements.

3.2 HPGe Detector Array

The high purity germanium (HPGe) detector array consists of 6 detectors elements; each is a planar p-type intrinsic germanium crystal with an active diameter of 10mm and an active depth of 10mm. The elements are arranged in linear array separated by 1.95cm center-to-center spacing and housed in an aluminum cryostat 14cm in diameter, manufactured by Princeton Gamma Tech, Inc. of Princeton, NJ.

The original design included six beryllium windows, 10.69mm diameter, in the aluminum casing positioned in front of the six detectors. The distance from the windows to the detector crystals was, and remains, 5.94mm. The former detector array geometry is pictured in figure 7.

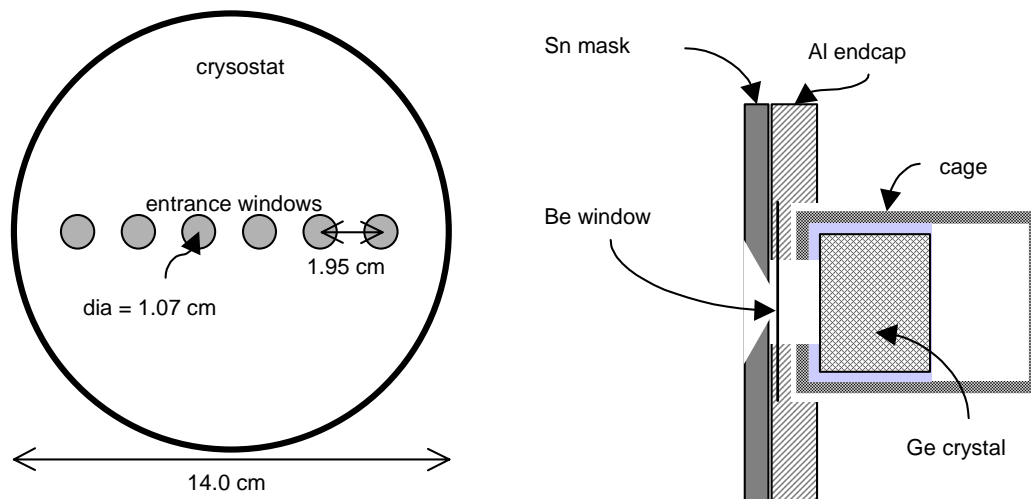


Figure 7: Narrow collimation, (left) view of detector array with six beryllium windows and (right) collimating tin mask and the detector housing (Evans, 1999)

The tin mask pictured above is designed to limit the area of the detector crystals exposed to inbound radiation. This effort was made to limit the number of partially absorbed events measured by the system. The tin mask is shown in figure 8.

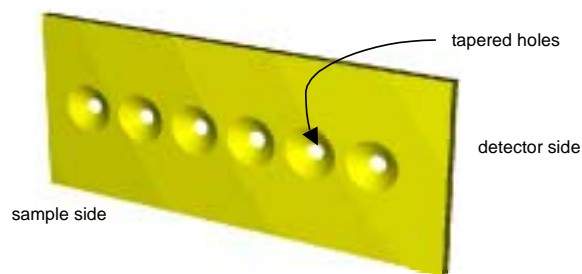


Figure 8: Tin mask with narrow collimation (Evans, 1999)

The modified detector assembly has a continuous beryllium window encompassing the faces of all six detectors and incorporates a tin mask of

dimensions equal to the new beryllium window. This allows the field of view of the detectors to be considerably larger increasing the detector throughput significantly. The original cage material was aluminum. The new cage is constructed from stainless steel, a higher Z material, to reduce the amount of photons scattered in the cage and then registering in the detectors. Because a photon scattered in the cage material, would contribute to noise, if detected, this decrease in the scattering cross-section subsequently reduces noise. The reduction of scattering present within the cage material will reduce the contribution of measured photons not having a energy to position relationship dependent upon the Compton equation. The layout of the system remains relatively the same and is pictured below.

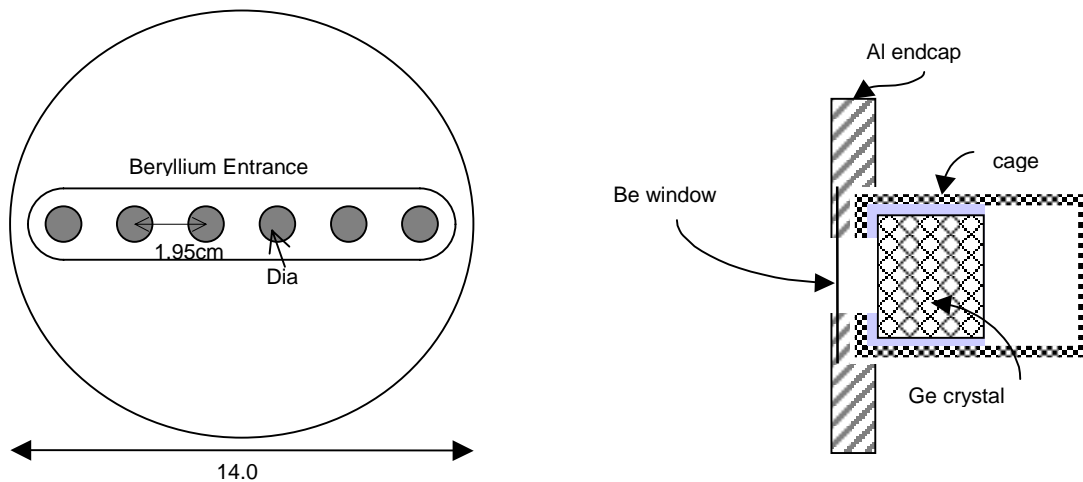


Figure 9: Wide field of view, (left) new beryllium window encompassing all six detectors in the array and (right) detector housing without the tin mask

The effect of the modified field of view upon the angular efficiency of the system is shown in the figure 10.

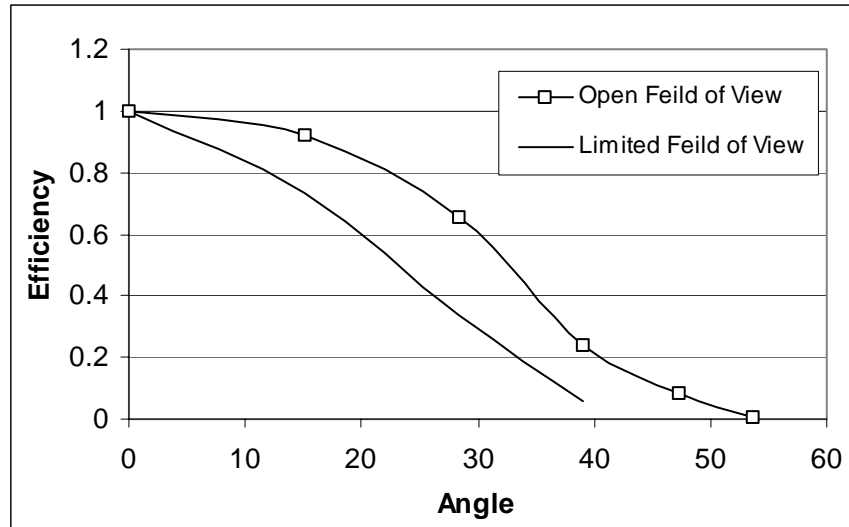


Figure 10: comparison of the efficiency as a function of angle (degrees) between the narrow field of view (Evans, 1999) and the wide field of view geometries for the detector array using 88keV photons

The limited field of view is a plot of the cubic polynomial used by Evans to fit the efficiency data. The wide FOV permits the detectors to have greater relative efficiencies at the angles where both geometries are able to register counts and it allows the detectors to register events out to 53 degrees while the narrow FOV is equal to zero at 43 degrees.

3.3 Data Acquisition

Signals from the detectors are processed with analog pulse shaping electronics, digitized in a multi-channel CAMAC standard CAEN C420 ADC. A Wiener CC16 CAMAC crate controller interfaces the CAMAC mini-crate ADC to a personal computer running Wiener's Multi_2 data interface software. The analog components' responses vary with time and cause a drift with respect to detector energy calibration. A schematic of the system is shown in figure 11.

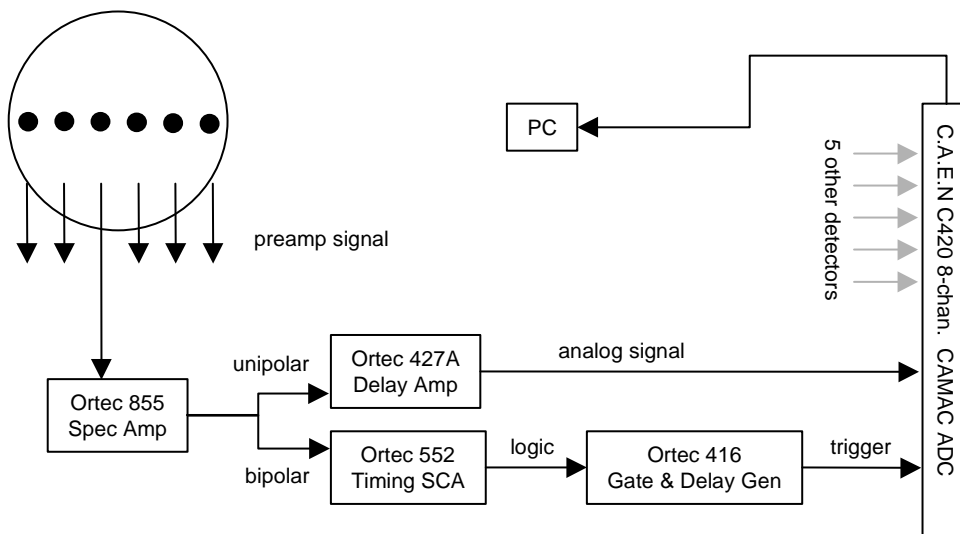


Figure 11: Pulse shaping electronics for the MCST system (Evans, 1999)

New CAMAC modules have been developed and acquired for this project. The new modules will replace the analog components of the system and eliminate the electronic drift in the system. Unfortunately, the modules and software do not support the Wiener CC16 crate controller and were not implemented in current experimentation.

3.4 ^{109}Cd Source

The selected source provides 88keV gamma rays. The mean free path in aluminum at this energy is 2cm, ensuring a large fraction of the incident gamma rays scatter in 0.5 to 1.0cm thick Al samples. Furthermore, there are no emissions above 88keV that would otherwise corrupt the single scatter spectrum in the energy range from 55 to 90keV. The intrinsic peak efficiency of HPGe detectors is approximately 100% from 55 to 90keV.

Ideal efficiency provides the convenience of representing the detector energy response as a Gaussian distribution and eliminates the need to remove an impulse response function. The half-life of ^{109}Cd is 1.27 yrs. Upon delivery, the activity of the source was 75mCi on 15 October 1999. The source was manufactured by Isotopes Productions Laboratories of Burbank CA. The active volume is contained in a model 3204 capsule, which is 8mm in diameter and 5mm in height. Elemental cadmium is plated on a silver substrate and protected by a beryllium foil window. The capsule design has been tested and registered in accordance with ANSI classification C33232 for sealed gauging sources. Pictured in figure 12 is the spectrum around the 88keV peak. Previous samples purchased from the same supplier have had significant contribution from contaminants. Peaks representative of contaminants are an order of magnitude smaller than the emission from the ^{109}Cd 88keV peak and are subsequently unobservable in the spectrum below.

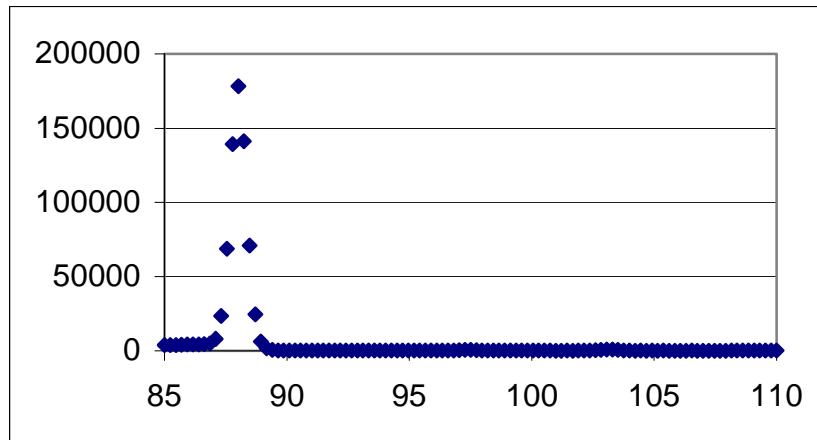


Figure 12: Spectrum for the ^{109}Cd source used during sample measurement, shows contamination peaks an order of magnitude smaller than the 88keV peak

Chapter 4: Results and Discussion

The primary focus of this work is the application of the MCST system to an aluminum sample including a steel rivet with the possibility of aluminum oxide corrosion eroding on the surface opposite the detector array. The top, bottom, left, and right edges of the sample are able to be defined for any given sample and will be implemented during reconstruction. The discretization method has been implemented to restrict the solution space of the system, thereby enabling the method to reconstruct discontinuous density transitions. Both the sample boundaries and the discretization method contribute to attaining more accurate electron densities and to reducing the artifacts along the edges of the samples. The field of view of the detectors has been widened increasing their throughput thereby allowing better signal-to-noise relationships for the same sampling period.

4.1 Rivet

The application of this imaging system is the detection of oxide development in aircraft. The typical aircraft will suffer from increased degradation of the airframe in the immediate vicinity of the steel rivets, which fasten the aluminum coating of the airplane to the frame itself. Corrosion of the more reactive aluminum is promoted at interfaces with less electropositive metals, iron etc. The addition of the higher Z steel rivet will effectively shield material located on the side opposite the source making detection of density

differences in the aluminum adjacent to the rivet more difficult than in its absence.

4.1.1 Rivet Sample

The sample used to represent a rivet in an aluminum frame is fashioned using machined pieces. This was done because the reconstruction code assumes a 2D imaging surface and therefore cannot reconstruct a curved surface as would be introduced by a real three- dimensional rivet. Surrounding the bottom of the rivet small areas of the aluminum where machined and small aluminum inserts where constructed which may be removed from the sample. During this study the aluminum inserts were removed to simulate an oxidized sample, while they were left in to simulate a solid sample. These cavities may also be filled with a gibbsite powder in order to simulate a more realistic oxide measurement; but, this was not done in this study.

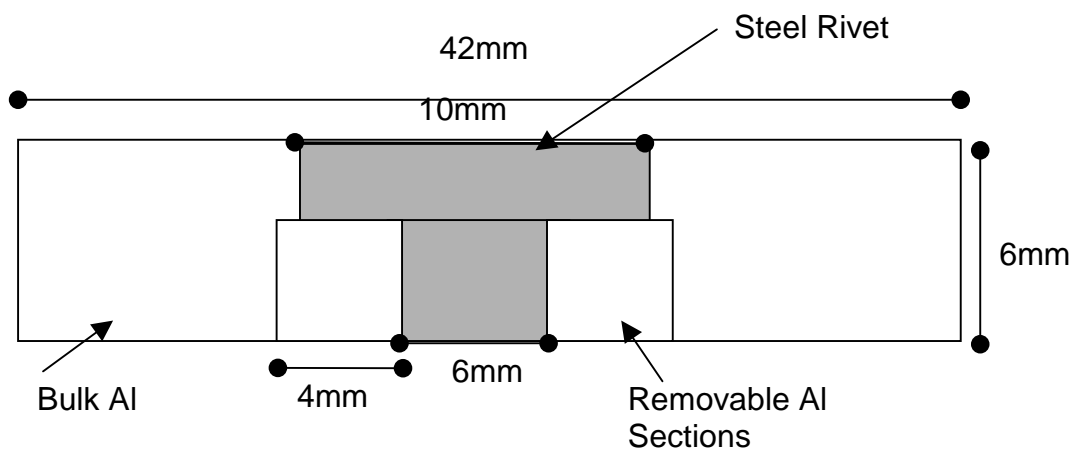


Figure 13: Sample simulating aluminum airframe surface including a steel rivet and corrosion

4.1.2 Measurement Geometry

The measurements are made with the source located only on one side of the sample. The rivet sample is imaged using both the wide field of view and the narrow field of view for the detectors.

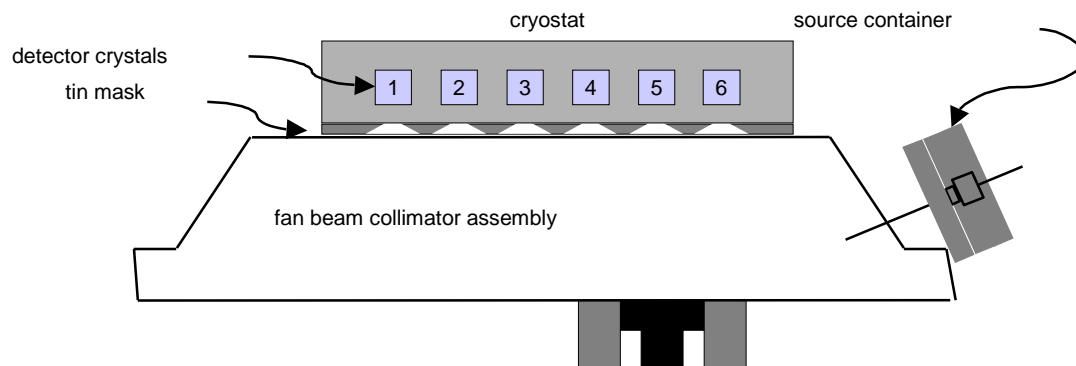


Figure 14: sampling geometry used for the rivet sample

Measurements taken from detectors 6, 5, and 4 in figure 14 are assumed to be identical to spectra from detectors 1, 2, 3 in figure 15 based upon sample symmetry. Therefore, the images are reconstructed simulating equivalent measurements taken with the sample located on the opposite side as pictured in figure 15.

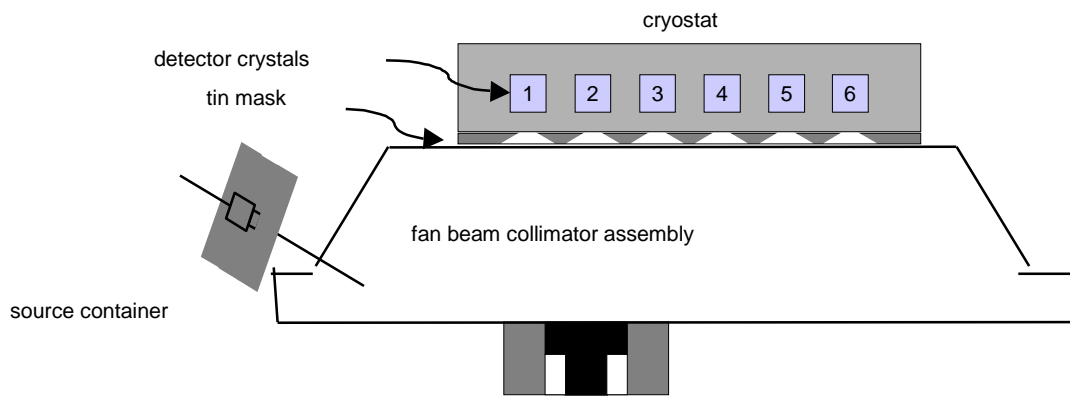


Figure 15: Second position for the rivet sample. Assuming symmetric results of the measurements made in the original position yields the spectra for this position

4.2 Initial Reconstruction

The reconstruction of the rivet sample, assuming no prior knowledge of sample location, is the starting point for this work. The location of the steel rivet will be assumed by not allowing the reconstruction algorithm to alter the electron density of any voxel initially input as iron. The sample will be surrounded, two voxels deep, on all sides by air. This is done to observe if the reconstruction algorithm is able to restrict the placement of sample electron density to the voxels where the sample truly exists or if it will smooth density into regions of void. This result will serve as a reference point for comparing effects of the

improvements made upon the image reconstruction during the course of this discussion. The image to be reconstructed should have the form of figure 16 and 17.

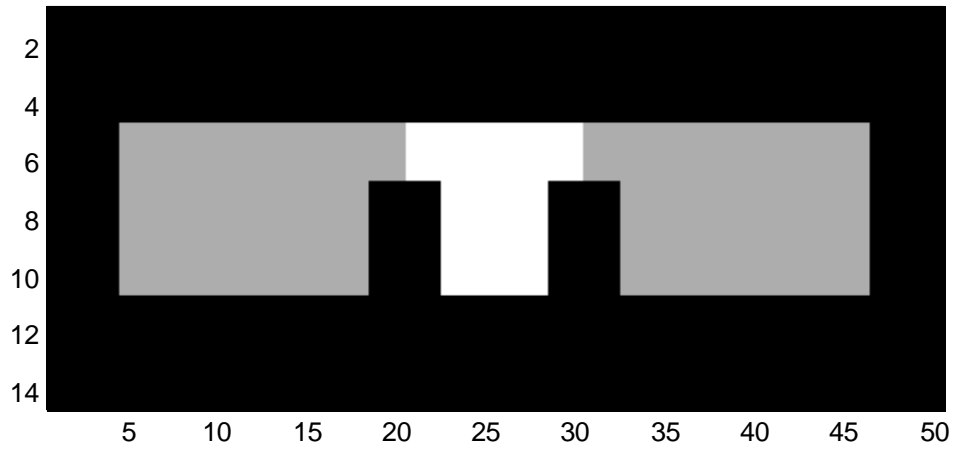


Figure 16: 2-dimensional projection of electron density map, x and y-axes map voxel coordinate while shade indicates density value.

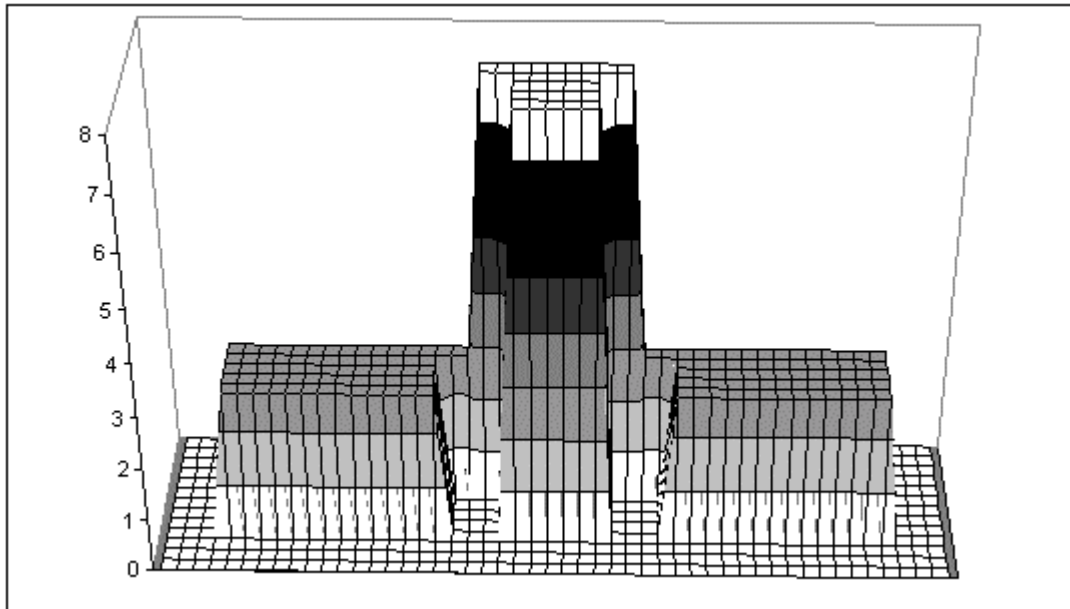


Figure 17: Image of the rivet sample, perfect density values. Height (left axis) is the electron density, for Al = 2.7, Fe = 7.3, Air = 0.0, shades show transition from integer numbers.

Figure 16 shows a two-dimensional projection of the reconstruction while figure 17 accentuates the density values attained during the reconstruction. The density of the steel rivet has been reduced in the 2D view in order to allow the contrast between the lower density values to be observed. Specifically note the width of the air surrounding the sample on all sides of the sample. The reconstruction algorithm will smooth the aluminum density into these regions.

The next image (figure 18 and 19) will use simulated spectra including no noise. The spectra have been scaled universally by 3.55×10^6 photons. This scaling factor was determined using a qualitative goodness of fit evaluation. Unfortunately, a uniform scaling factor has proved insufficient for matching simulations with measured data therefore additional scaling factors have been used per detector. (Included in appendix A).

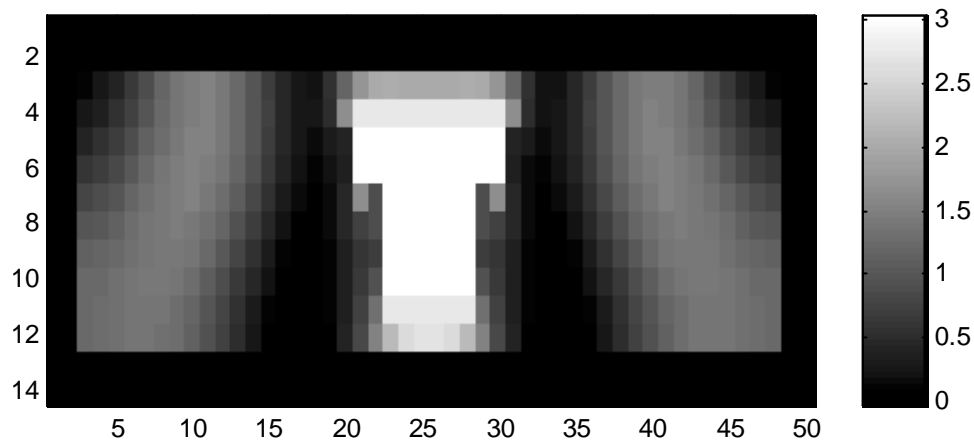


Figure 18: 2-dimensional projection of electron density map using simulated spectra, x and y-axes map voxel coordinate while shade indicates density value.

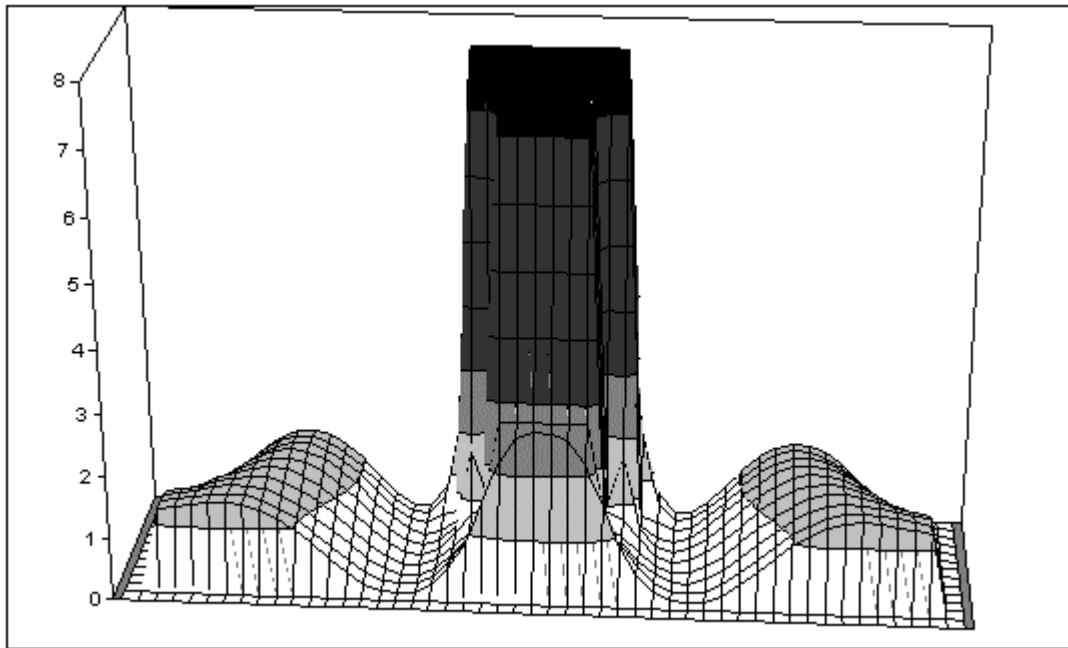


Figure 19: Image reconstructed from simulated data, no assumptions about boundaries, Height (left axis) is the electron density, for Al = 2.7, Fe = 7.3, Air = 0.0, shades show transition from integer numbers.

By considering both representations of the image, one may ascertain that the reconstruction places aluminum density on both the top and the bottom of the rivet. This is clearly not a physical result. Furthermore, the densities attained in the bulk of the sample are less than 1.5 whereas the electron density of aluminum is 2.7.

The measured spectra will now be used to reconstruct the rivet. Comparisons of the simulated spectra to the measured spectra are shown in figure 20.

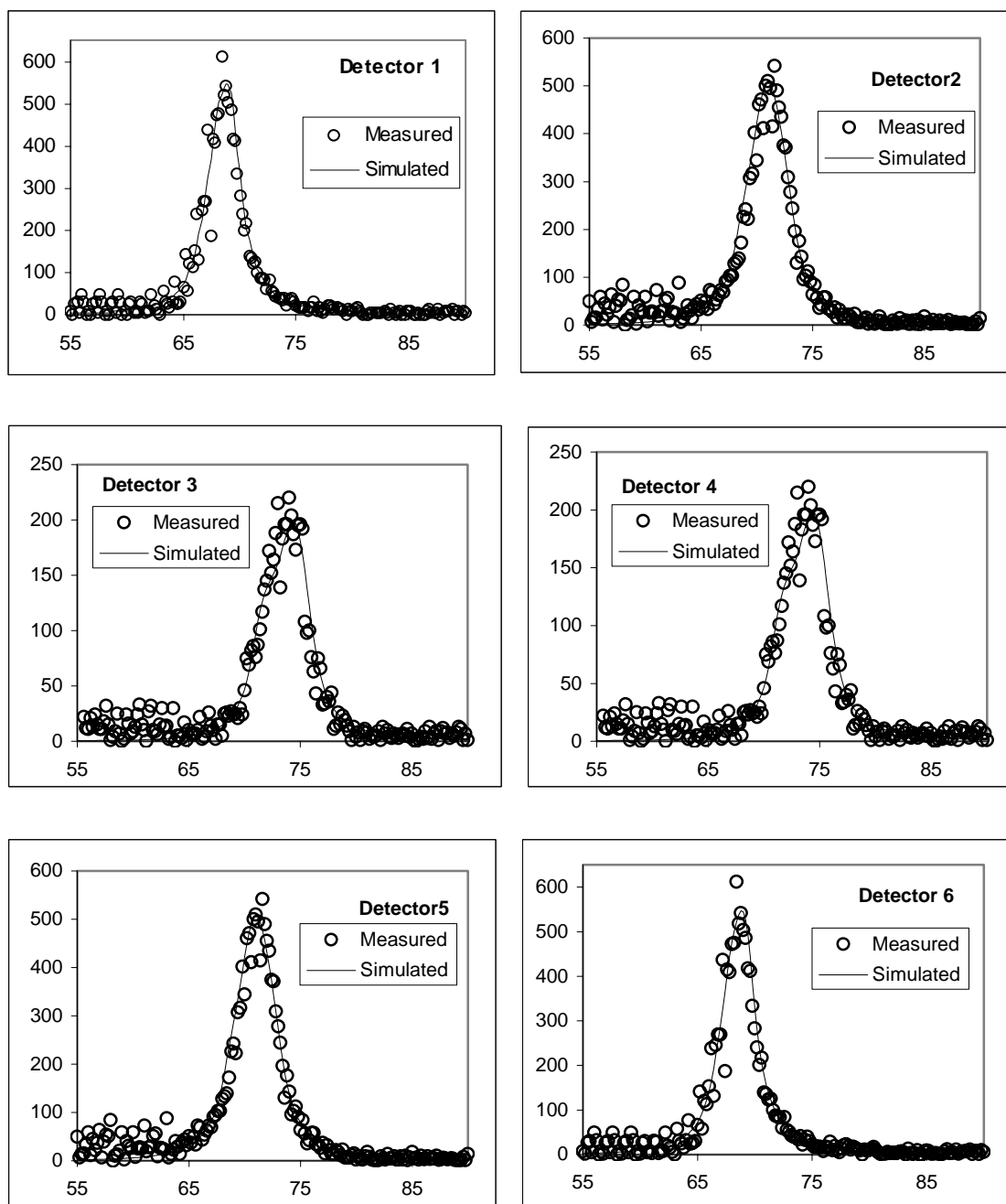


Figure 20: Comparison of simulated to measured spectra, counts (arb. Unit) vs. Energy in keV

The reconstruction of the rivet from measured data is shown in figure 21 and 22.

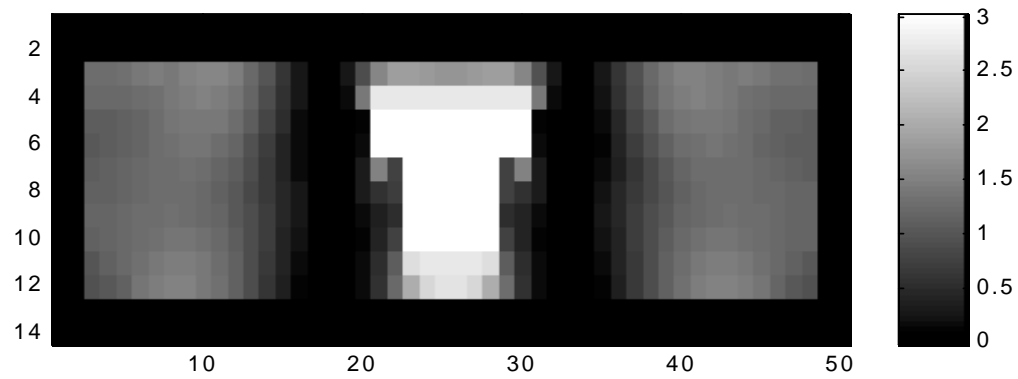


Figure 21: 2D projection of electron density map from measured data, no assumptions about boundaries, x and y-axes map voxel coordinate while shade indicates density value.

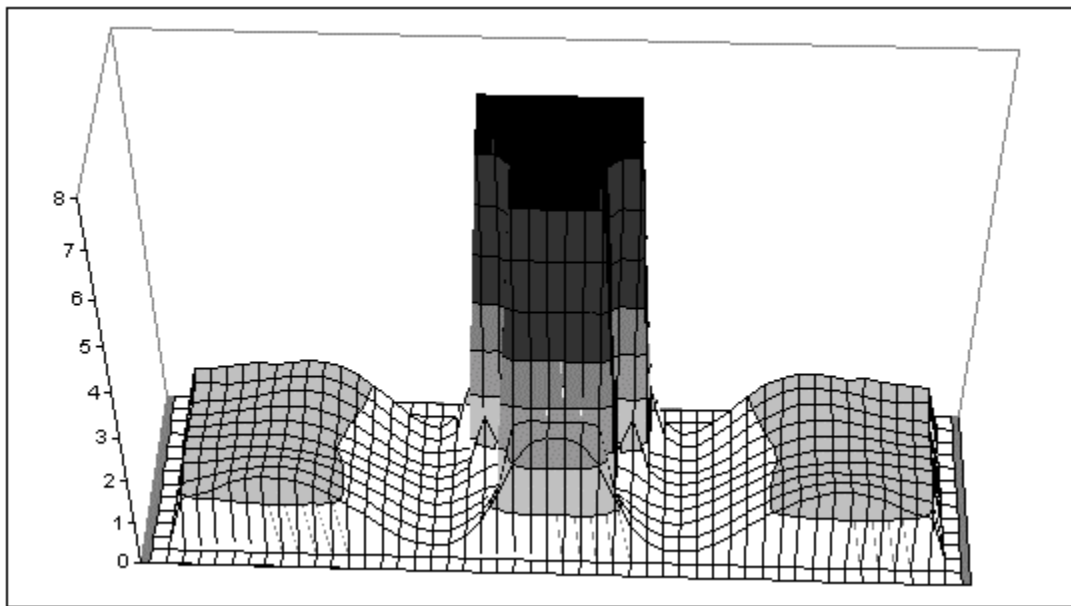


Figure 22: Images from measured data, no assumptions about boundaries, Height (left axis) is the electron density, for Al = 2.7, Fe = 7.3, Air = 0.0, shades show transition from integer numbers.

The images reconstructed from simulated data and the measured spectra are similarly flawed. Both reconstructions reduce density of the aluminum from 2.7 to less than 1.5 and place aluminum above and below the rivet. Furthermore, the

aluminum has been spread throughout all the voxels where density may be placed by the reconstruction algorithm giving the user the impression that there is aluminum density in areas where there is no material at all.

By applying constraints upon the reconstruction algorithm one may acquire more accurate values and localities for the sample densities.

4.3 Sample Boundaries

During previous image reconstruction, the edges of the sample were assumed to be unknown. This assumption allows the smoothing term, included in PWLS, to reduce the electron densities of the voxels where aluminum is present in the sample and incorrectly assign electron density to voxels where air is present. There is no need to allow ambiguity concerning the sample boundaries for they may be determined.

4.3.1 Boundary Specification

The top boundary of the sample may be determined using a physical finger system or a laser-based system similar to positioning system used by Zhu (1995), thereby allowing the reconstruction algorithm to be implemented with a specific top boundary.

It is postulated that the intensity of photons incident upon the detectors will be related to the amount of material present in the sample. Therefore, if evaluating sample of the same dimensions with the exception of depth one may approximate the depth of the samples by comparing the measured intensity to a

detector response function determined using aluminum samples of varying thickness. Four aluminum samples have been used in this calibration.

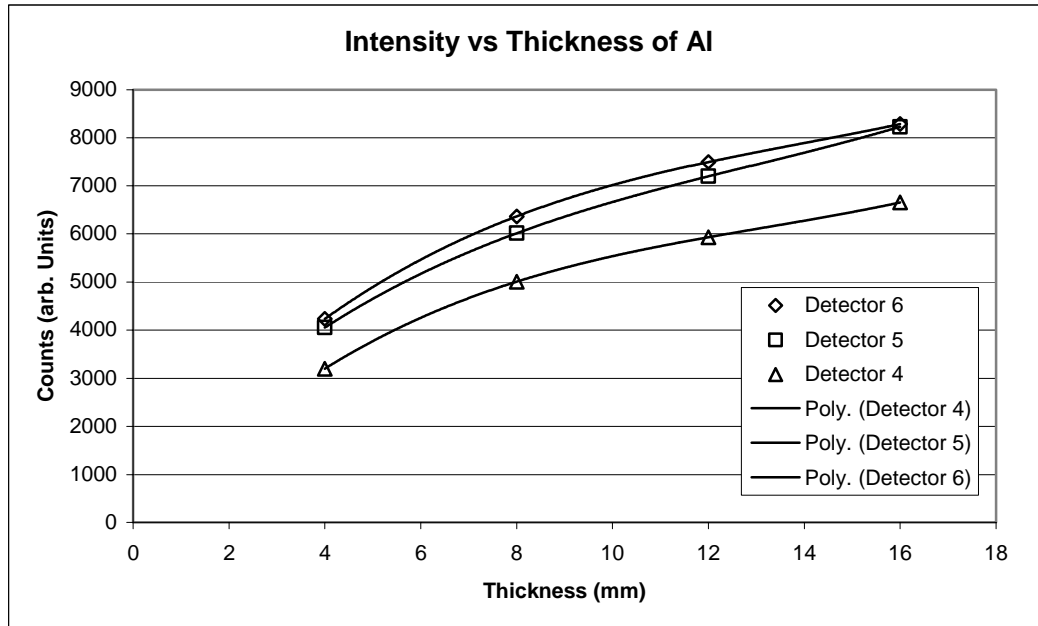


Figure 23: Number of counts from 55 to 90keV over 14,000 secs, as the thickness of Al varies from 4 to 16mm

Samples 1,2,3, and 4 varied in thickness from 4, 8, 12,and 16mm respectively. The measurements were taken for 14,000secs. The counts are summed over the energy range of 50keV to 90keV. Cubic polynomials are fit to these data points and shown above. The polynomials are used in order to determine the depth of the samples used throughout the remainder of the paper. The data needed for the thickness determination is already collected in order to image the sample; thus, without the necessity of making any further measurements the back edge of the sample may be determined without ambiguity.

In the case of the rivet sample, some scaling factors exist between the data collected while sampling the Al samples and the rivet samples. The most obvious of these differences is that the rivet samples were measured for 99,999sec, the maximum time allowed by the multi software, while the aluminum samples were measured for 14,000 sec. The ratio of these two values is approximately 0.14 and is the first scaling term. The second difference between the two measurements is the detector collimation used during the measurement. The rivet samples were measured with the narrow field of view and the aluminum depth samples were measured with the wide field of view. This scaling is approximately 2.2 as derived by comparing the rivet results with the two fields of view. Counts were summed from 55 to 90keV for each detector and the sample depth was determined, using the cubic polynomials for each detector. Detectors 6, 5 and 4 returned thickness values of 6.1, 6.2, and 4.8mm respectively. Because voxel sizes are 1mm square, the values in the tenths places are of no concern showing that either detector 5 or 6 will yield the correct depth for the given sample geometry. Detector 4 has given a much smaller value, which is a direct result of the existence of the rivet. Photons traveling from the source to detector 4 primarily pass through the steel rivet. Therefore, the rivet's effect upon this detector is much greater than in the other two. The existence of oxide within the sample may also have an effect upon this determination. Therefore to compliment the earlier results, which were the result of the rivet sample with the voids on the opposite side of the sample, sample thickness has been determined

using measurements with a sample having no voids. The results for detectors 6 and 5 are 5.8 and 5.6mm respectively showing that the sum of the counts over the energy range from 55 to 90keV is sufficient to determine the correct thickness with or without the inclusion of the voids. Having determined the upper edge of the sample by physical means and the back edge by fitting the summed counts to the empirical depth determining polynomial, it is time to pursue the determination of the sides of the sample.

The edges of the sample area are derived from the source collimation existent in the MCST measurement apparatus. The MCST program applies user-defined lines in order to determine which voxels, in the sample, are illuminated by the radioisotope. The collimation is shown in the diagram below. The aperture line pair d1 and d2 bound the region of the aluminum sample, which is illuminated, by the gamma source.

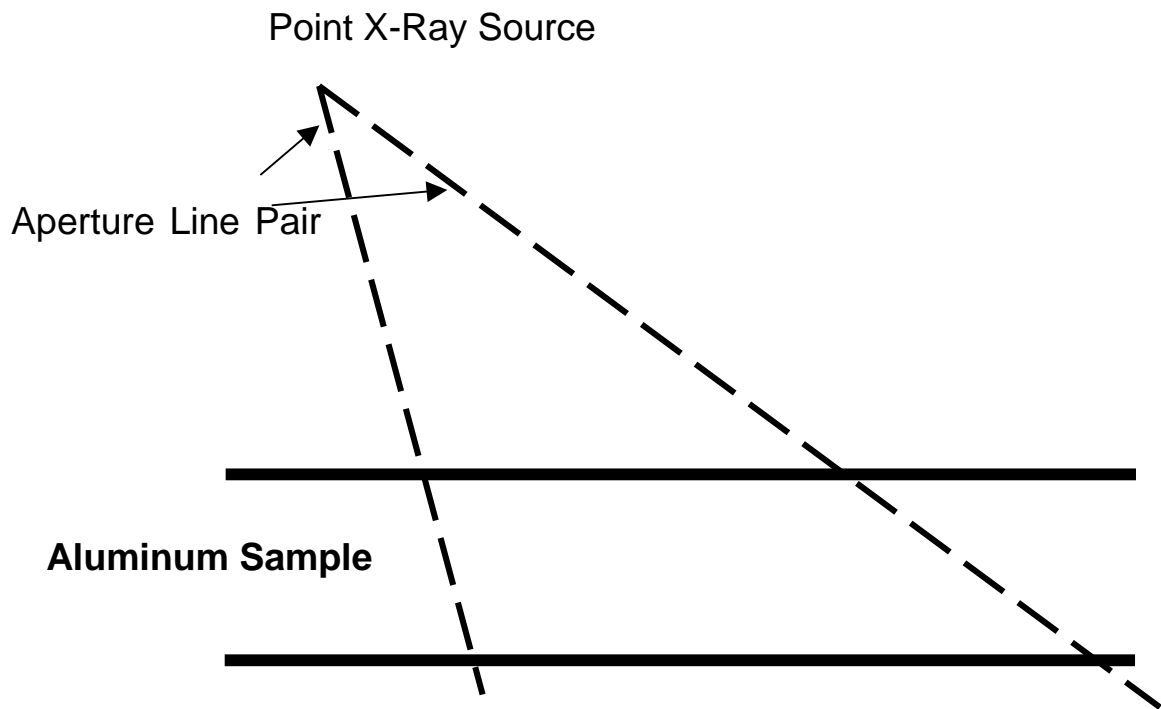


Figure 24: Illustration of the collimation parameters required for the execution of ScatGram(Costescu)

If a voxel is not illuminated, no singly scattered photons will originate from that volume element; thus, no information concerning the electron density of the unilluminated voxels are contained in the spectra. PWLS will not alter the density values for the unilluminated voxels from the initial guess. These voxels may be given fixed densities and thereby not considered as variable when reconstructing the images. Now that all of the sample boundaries have been determined, the sample densities will no longer be smoothed into the surrounding air.

4.3.2 Application of Boundaries to Rivet Sample

Figures 21 and 22 show the image of the rivet sample assuming that the boundaries are unknown. Boundaries will now be introduced during image reconstruction and the effect will be reported. Figures 25 and 26 are images of the sample including the top boundary

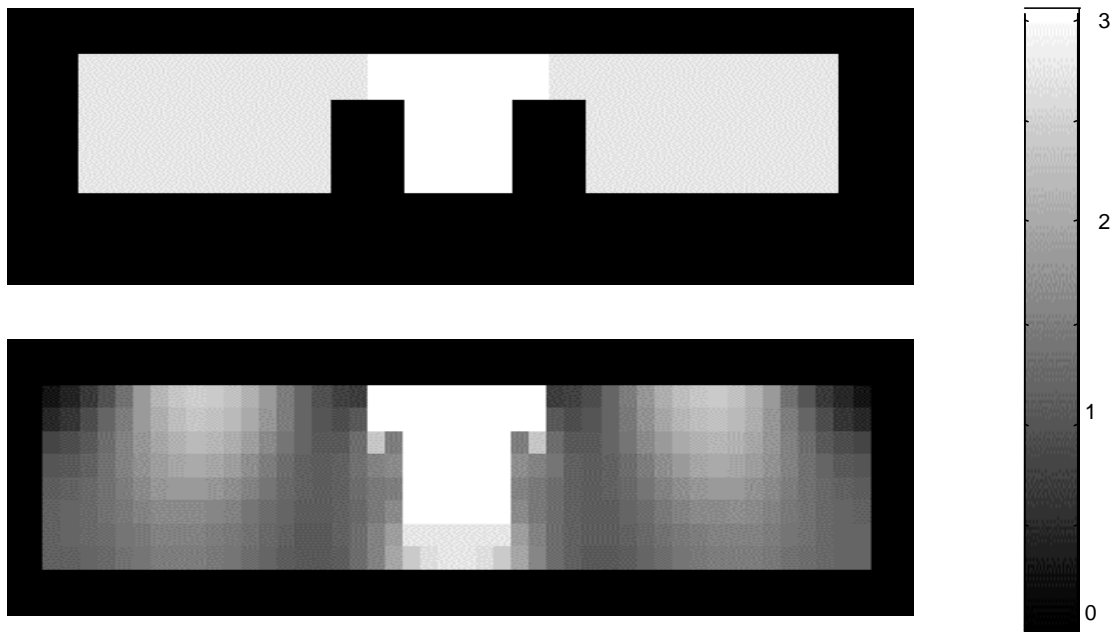


Figure 25: 2D projection of electron density map (Top) plot of actual sample and (bottom) reconstruction from measured data, assuming top boundary is known, x and y-axes map voxel coordinate while shade indicates density value.

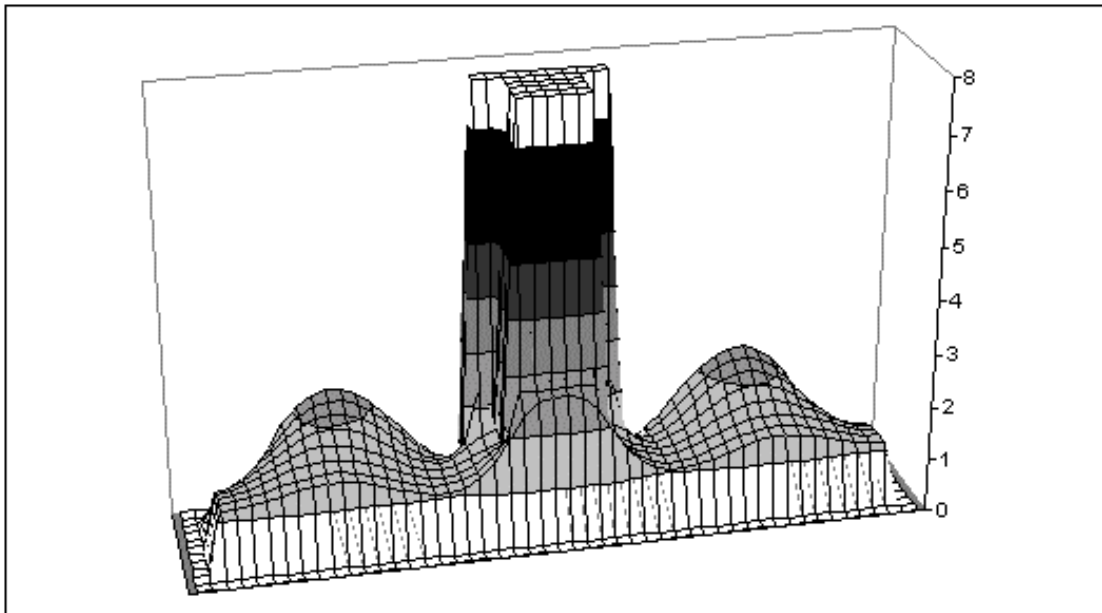


Figure 26: Image of rivet reconstructed assuming the top boundary is known, Height (left axis) is the electron density, for Al = 2.7, Fe = 7.3, Air = 0.0, shades show transition from integer numbers.

The inclusion of the top boundary has eliminated the incorrect placement of electron density located upon the top of the rivet. Additionally, the regions to the left and right of the rivet are peak at just above 2.0, which is closer than 1.5 to the 2.7 density mark, the correct value for aluminum.

Using the sample thickness determined using the depth algorithm is section 4.3.1, the bottom boundary will be place 6mm below the top surface. The inclusion of bottom as well as the top boundary yields the following image (figure 27 and 28).

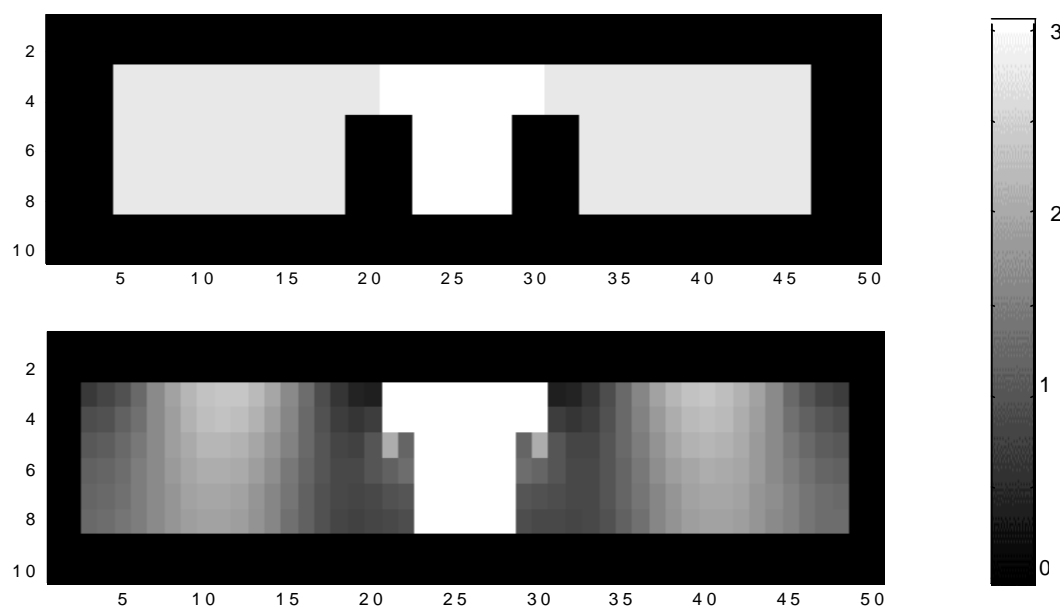


Figure 27: 2D projection of electron density map (Top) plot of actual sample and (bottom) reconstruction from measured data, assuming top and bottom boundary is known, x and y-axes map voxel coordinate while shade indicates density value

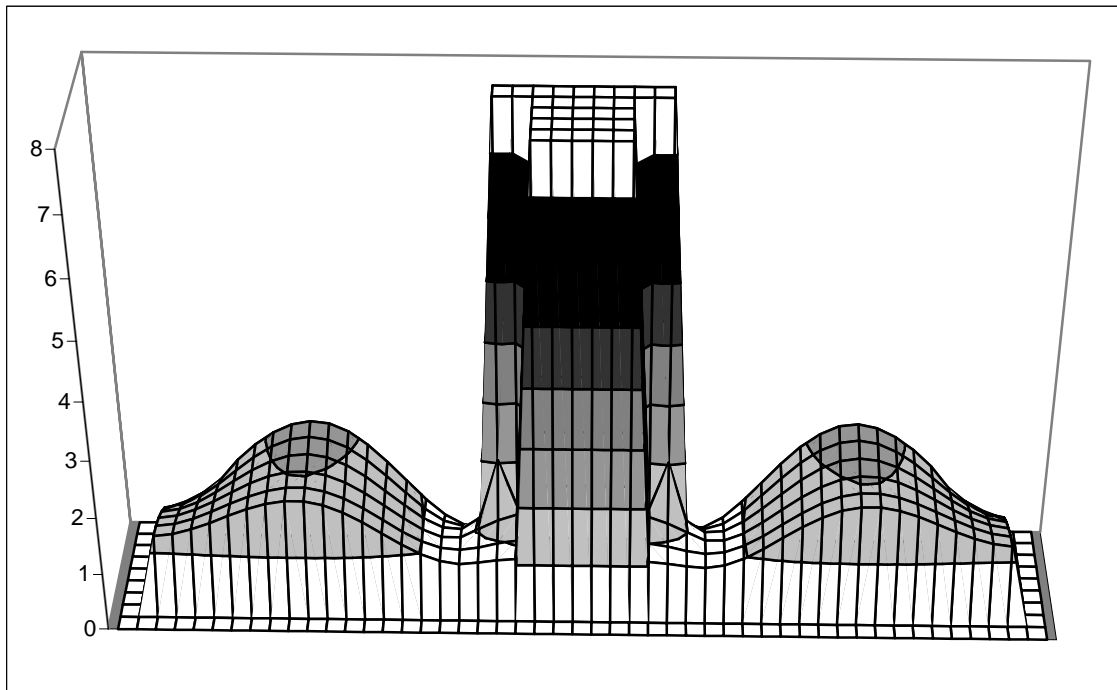


Figure 28: Image of rivet including top and bottom boundaries, Height (left axis) is the electron density, for Al = 2.7, Fe = 7.3, Air = 0.0, shades show transition from integer numbers.

The inclusion of the second boundary has corrected the electron density on the underside of the rivet. Also, the areas of the sample adjacent to the shaft of the rivet and the 2 voxels on the left and right of the sample are approaching the correct density values, zero.

It has been shown that the inclusion of the top and bottom boundary of the sample eliminates the artifacts along the edges of the sample and encourages the electron density values to be more representative of materials present within the sample. Because no measurements using a source illuminating only small portions of the sample have been made, the effects will be examined using simulated spectra. The image reconstructed from simulated spectra of the rivet pictured in figure (15) made no assumptions concerning sample boundaries.

With the inclusion of both the bottom and the top boundary the resultant image is figure 29 and 30.

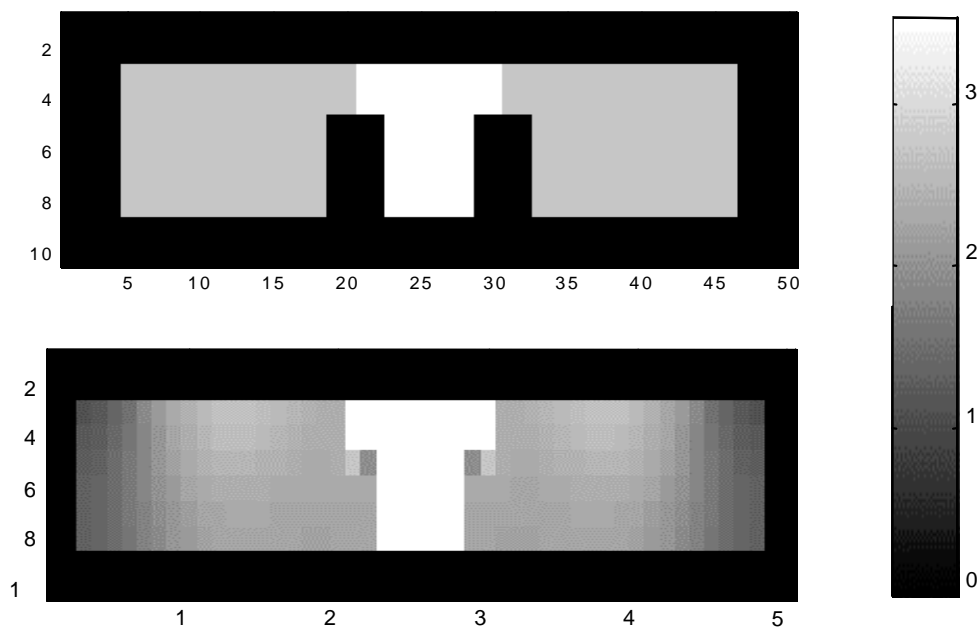


Figure 29: 2D projection of electron density map (Top) plot of actual sample and (bottom) reconstruction from simulated data, assuming top and bottom boundary is known, x and y-axes map voxel coordinate while shade indicates density value

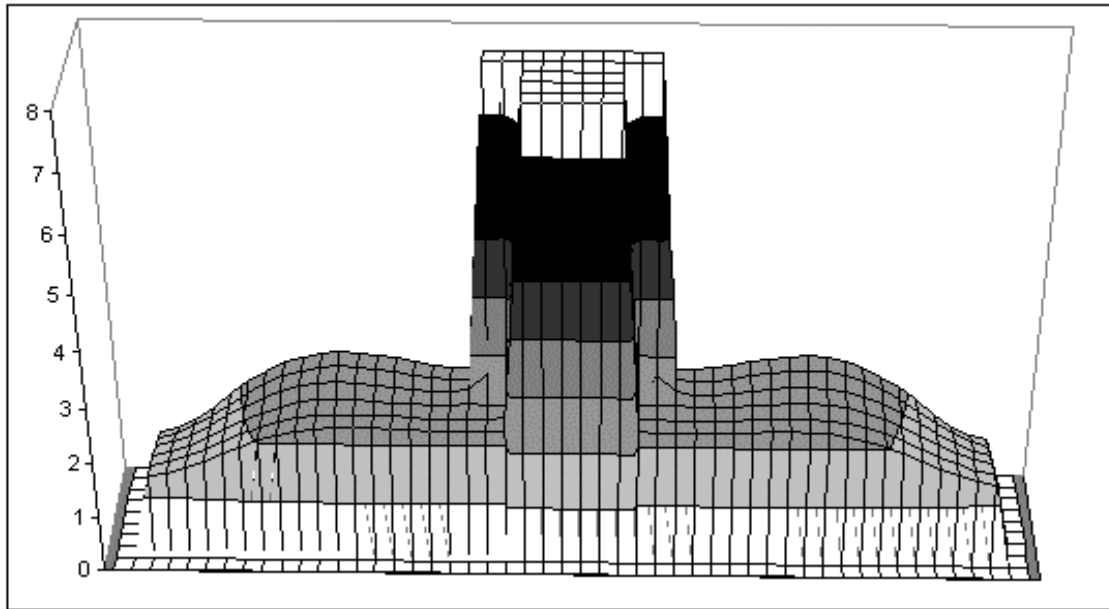


Figure 30: Reconstruction of rivet from simulated data, assuming both top and bottom boundaries are known, Height (left axis) is the electron density, for Al = 2.7, Fe = 7.3, Air = 0.0, shades show transition from integer numbers.

The aluminum areas of the sample have attained density values of approximately 2.7, improved from values less than 1.5. The voxels on the left and right of the sample decrease due to smoothing of bulk electron density into the surrounding air. The voxels near the rivet, although less than the aluminum surrounding them are not representative of the zero density, which is present in the sample. The collimation of the source will be adjusted so that the only portion of the sample illuminated is that along the shaft of the rivet. (shown in top image figure 31). It is important to emphasize that when two materials, such as steel and aluminum, are brought into contact the area at most risk of corrosion is the junction of the two materials. Therefore, it is not unreasonable to image implementing a system

which interrogates only those voxels directly surrounding the rivet. The illumination is as pictured below accompanied by the resultant images. The illuminated voxels are the only voxels the reconstruction algorithm is permitted to vary.

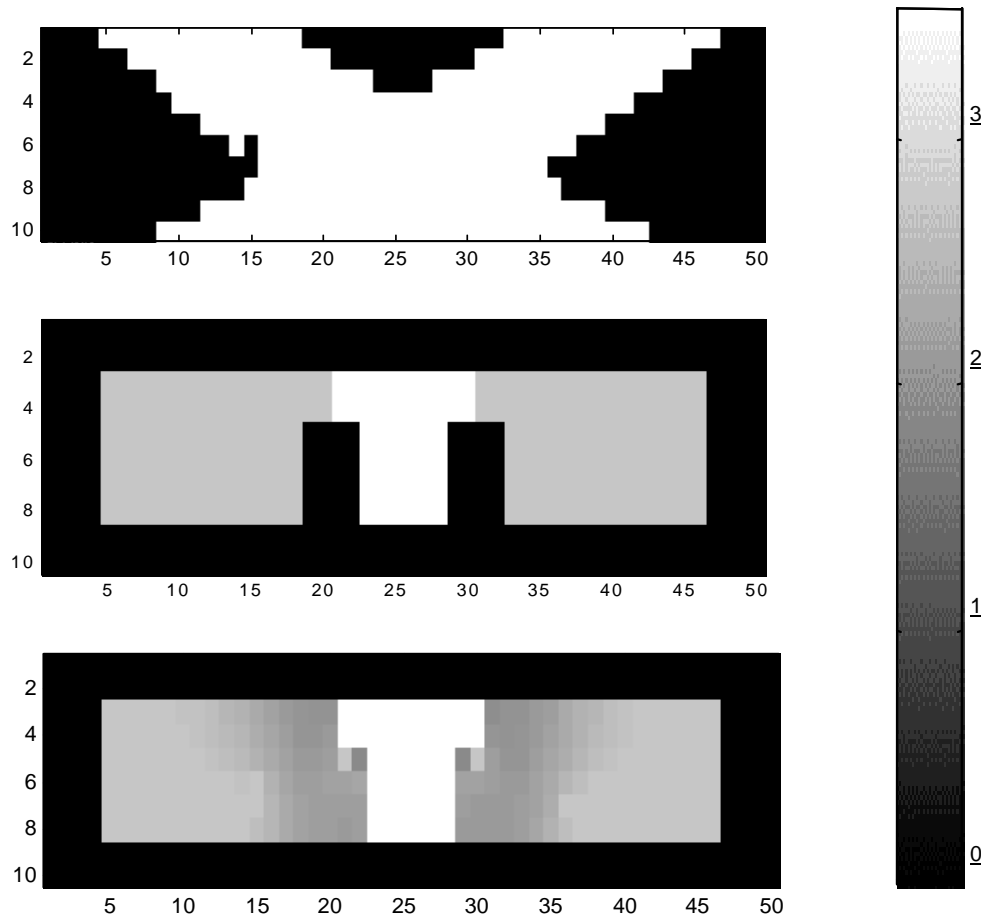


Figure 31: (Top) illuminated voxels are white while voxels not in inspection region are black, 2D projection of electron density map (Middle) plot of actual sample and (bottom) reconstruction from measured data, assuming top and bottom boundary is known, x and y-axes map voxel coordinate while shade indicates density value

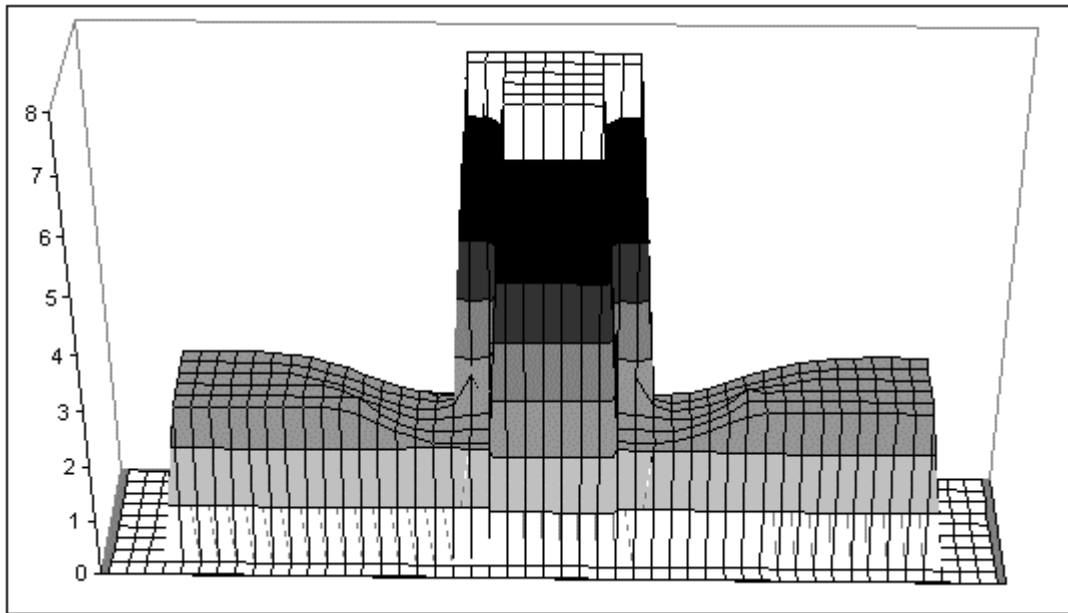


Figure 32: image of rivet from simulated data, assuming top, bottom and the left and right boundaries are known, Height (left axis) is the electron density, for Al = 2.7, Fe = 7.3, Air = 0.0, shades show transition from integer numbers.

This reconstruction has placed the void at the aluminum/rivet boundary and has not smoothed any of the aluminum density into the surrounding voxels. The ability to determine the left and right edges of the samples will be extended to all following reconstructions. Although the following reconstructions involve samples that were entirely illuminated, left and right boundaries will be fixed in light of the knowledge that in a real, extended sample the illuminated edges would be explicitly determined by the collimation of the source.

4.4 Smoothed Measurements

Inclusion of sample boundaries has improved the value of bulk electron densities reconstructed and eliminated artifacts along the edges of the sample.

Still, the density values in the vicinity of the rivet are approximately 1.2 instead of 0.0 and the void has been smoothed to the upper surface of the sample as well as on the bottom surface. In order to attain a higher level of image fidelity, a signal-smoothing step has been added previous to the reconstruction. The measured spectra have been smoothed using a moving average smoothing term in order to match the simulated and measured spectra with the effect of eliminating the remaining artifacts. A five-point average has been used resulting in the spectra shown in figure 33. The relative variance of a point that is the sum of five measurements will be less than the original measurement. (Knoll)

Because the variance is used as the weighting term in PWLS, these values must be adjusted accordingly during image reconstruction.

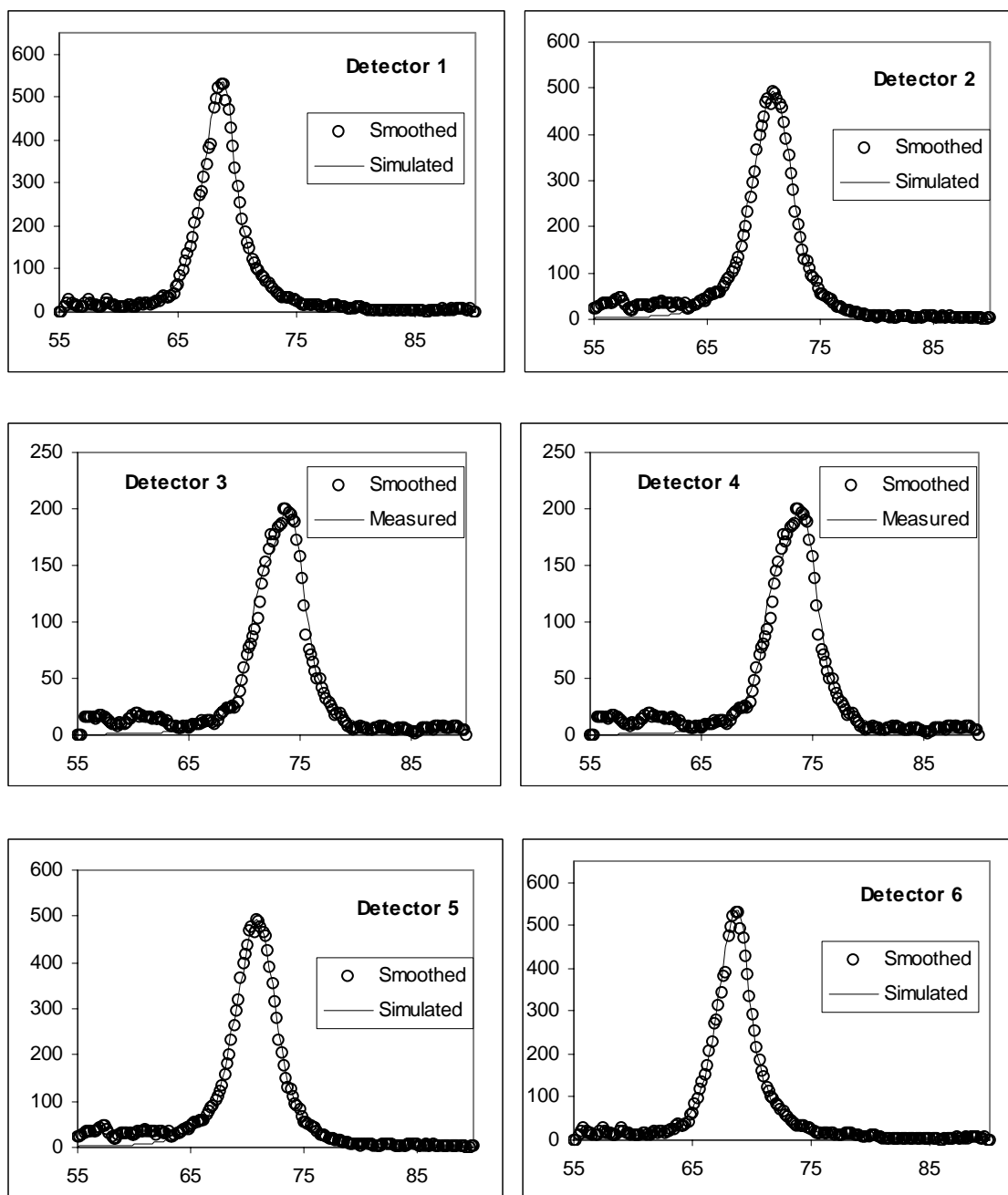


Figure 33: Comparison of smoothed measurements to the simulated spectra, counts (arb. units) vs. energy (keV)

Although smoothing the spectra served to reconstruct the upper voxels correctly, the voxels on the back of the sample have still remained at densities higher than

present in the sample. In the previous images the reconstruction algorithm has been iterated five times. The beta term in PWLS, equation 8, has been 2.5 for the first four iterations and then decreased to 1.5 during previous reconstructions. Relaxation of the smoothing term by reducing the weighting factor to 1.0 for the first 2 iterations 0.5 for the second 2 and 0.2 for the final iteration will allow the voxels to attain lower densities while the neighboring voxels remain at higher densities. The differences in the two reconstructions are pictured below in figure 34.

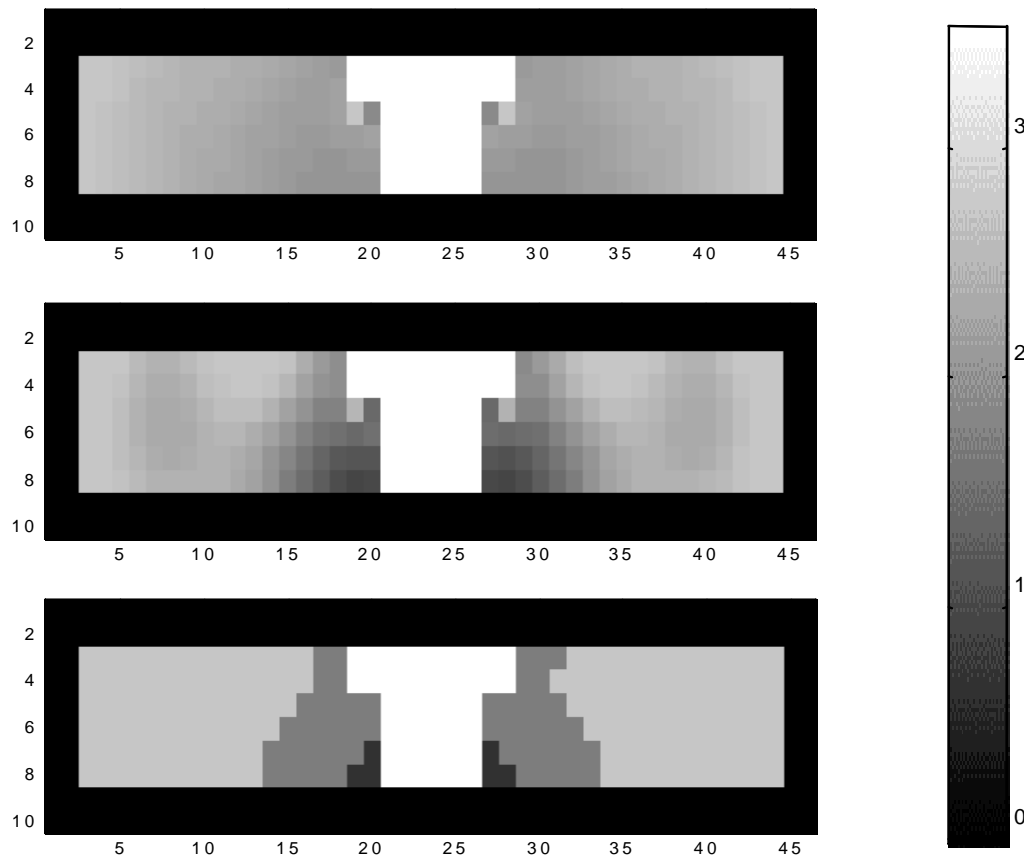


Figure 34: Reduction of beta to allow PWLS to converge to lower densities where appropriate and discretization code including fixing the voxels to discrete densities known to exist in the sample and allow discontinuous changes in density

The relaxation of the smoothing term has allowed the density values to approach zero around the base of the rivet while the voxels further out maintain values close to 2.7 for aluminum. The third image included is the result of the discretization code. The discretization code requires that the voxels take on values, which the experimenter has *a priori* knowledge. In this particular case the voxels are restricted to values of 7.8 for iron, 2.7 for aluminum, 0.0 for air, 1.7 for gibbsite and 0.7 for extreme states of corrosion.

The discretization step need not be implemented purely as a post-processing mechanism; however, it does require an image as input. The discretization step was applied at the end of each outer iteration. Unfortunately, PWLS is unable to diverge, to a measurable degree, from the initial density values, in one iteration. Therefore, applying the discrete code every iteration returns the initial guess invariably. Therefore, the discretization step was called every two, three, four...eight iterations. These results were then compared to the result of applying the discretization code after PWLS. There is no discernable difference between the two results and thus, no motive to implement discretization in any other way than as a post-processing step.

4.5 Widened Detector Field of View

A major limitation of the MCST imaging system is the amount of time required for sample collection. This length of time is driven by the requirement of

high signal to noise ratio required for the system to reconstruct images. In light of this need it was proposed by Evans that the field of view of the detectors be widened thereby increasing the detector throughput. The goal is to detect more photons per time interval and attain greater signal in less time.

4.5.1 Equipment Geometry

The field of view (FOV) of the detector array has been widened by the replacement of the tin collimation plate. The original design utilized small circular apertures while the new design is a long opening allowing the detectors to view more of the sample.

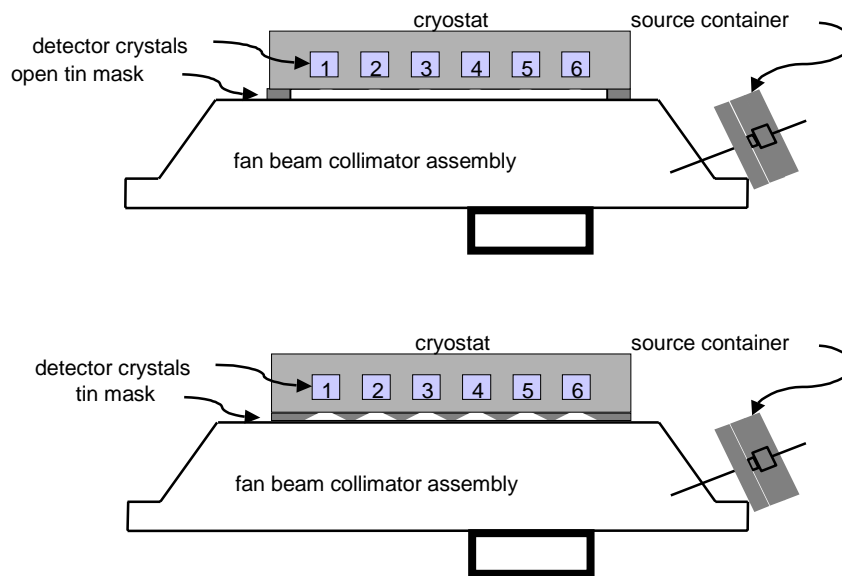


Figure 35: (Top) geometry of the dewtector array when the wide field of view is used and (bottom) the detector geometry when the narrow field of view plate is in front of the detector array

In figure 35 the detector array with the two different tin plates is pictured. The implementation of the new collimating plate increases the detectors relative efficiency as a function of angle, shown in figure 10.

The effect, of opening the FOV for detector 6 and 5, is shown in figure 36 and 37.

Simulated spectra were scaled by a global factor of 8.3×10^6 photons. The beta values during reconstruction are 2 iterations at each value 1.0, 0.5, 0.2 over six total iterations. Both the wide and narrow FOV measurements were taken over the same period of time (27 hrs.), geometry, source strength, and with the rivet void discussed in the previous discussion.

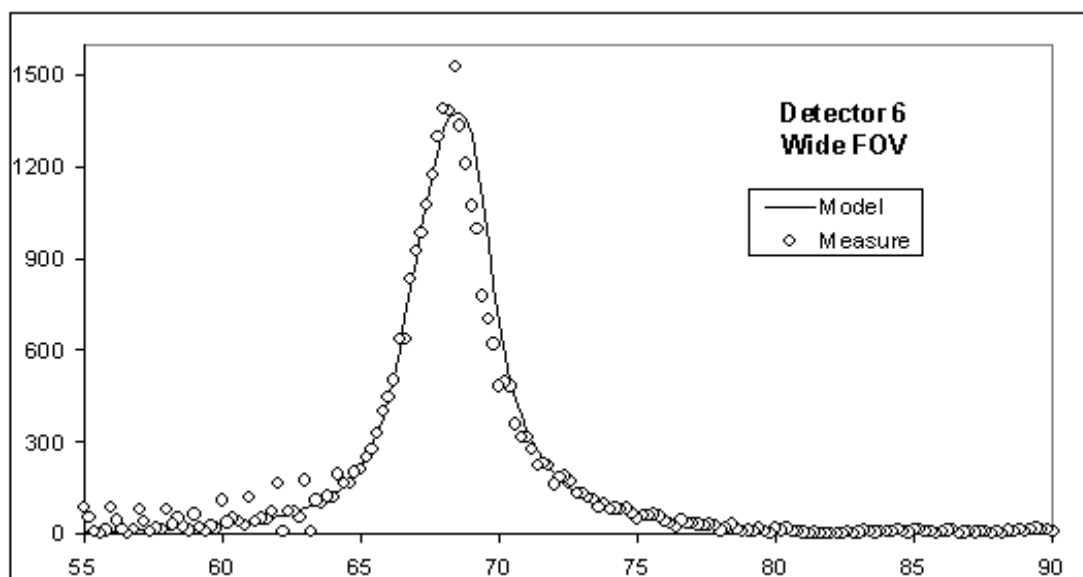
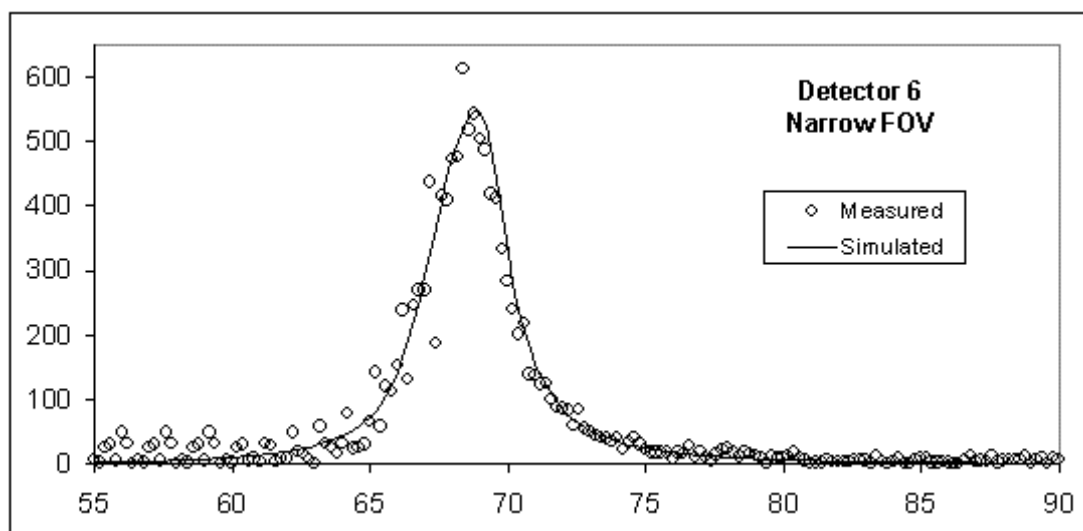


Figure 36: The measured and simulated spectra for wide and narrow field of view for detector 6, counts (arb. Units) vs. energy (keV)

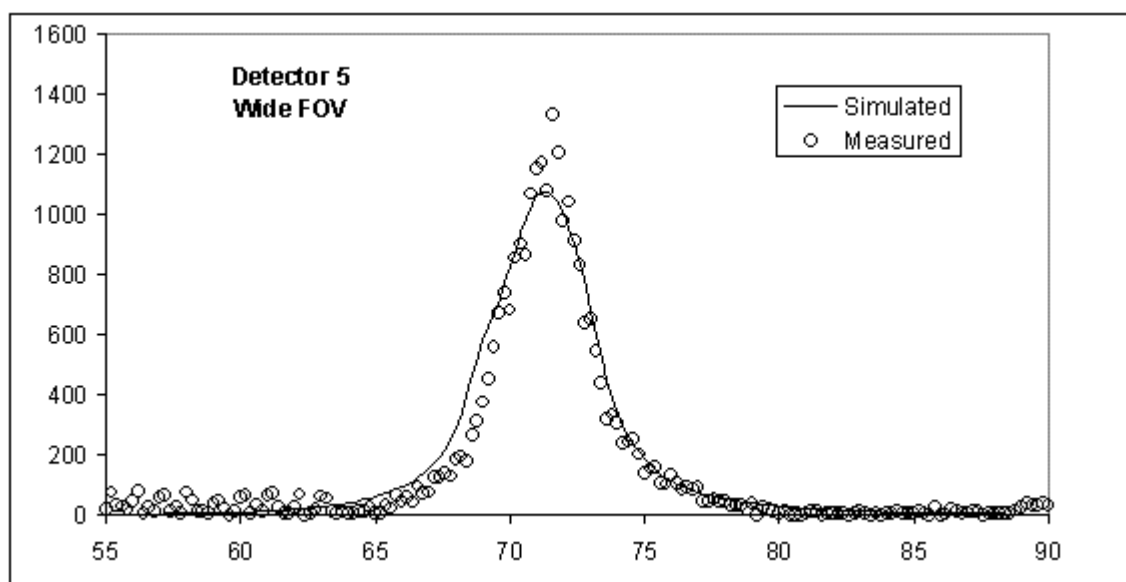
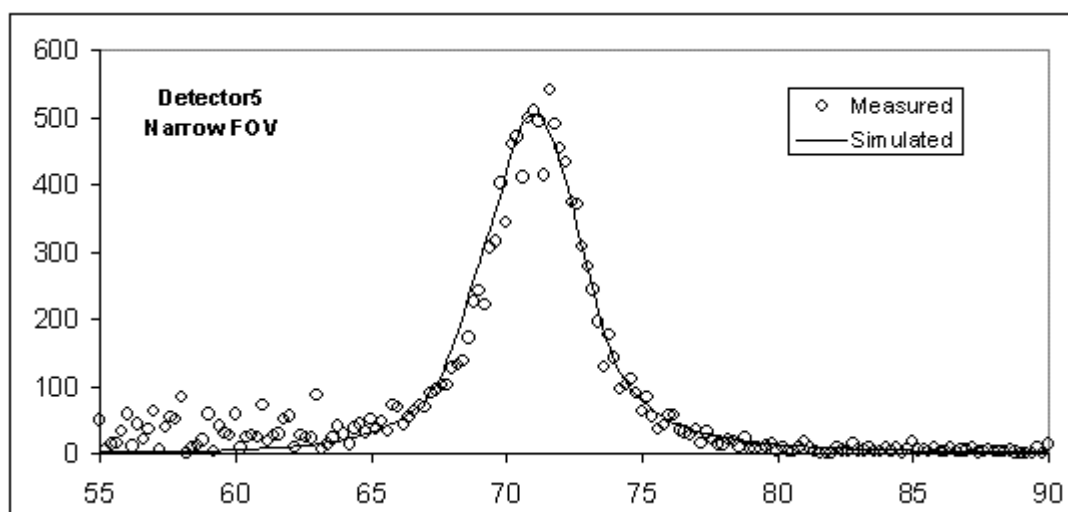


Figure 37: The measured and simulated spectra for wide and narrow field of view for detector 5, counts (arb. Units) vs. energy (keV)

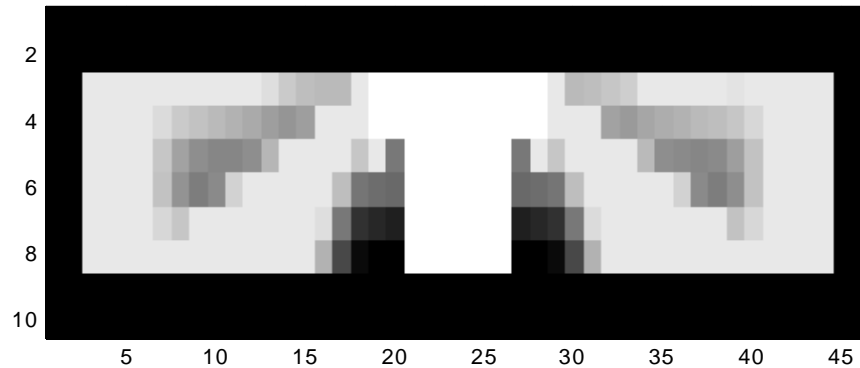


Figure 38: 2D projection of electron density map (Top) plot of actual sample and (bottom) reconstruction from simulated data, assuming all boundaries are known, using wide FOV, x and y-axes map voxel coordinate while shade indicates density value

Figures 36 and 37 display both the wide and narrow fields of view to accentuate the differences in the two measurements. The measurements using the narrow FOV are noisier, allowing the simulations to be scaled in order to bisect the measurements. The wide FOV improves the statistics of the measurements reducing the amount of noise in the spectra. Subsequently, the simulations are denied the liberty of bisecting the variance between measured data accentuating the divergence of the simulations from the measured results.

In both detectors five and six, the simulated peak has a greater full width at half max than do the corresponding measurements. Furthermore, a shoulder is developing upon the low energy side of the single scatter peak. This flaw is not observed in simulations of pure aluminum samples. Therefore, the most probable cause of this feature is inaccurate inclusion of the steel rivet in the predictive code.

The explanation of the divergence of the measurements from the simulations are not complete. An exhaustive study of the impulse response for the wide FOV geometry must be performed previous to any speculation on the topic. An important contribution, having yet to be studied, is the contribution of multiple scattered photons. The contribution for the narrow FOV has been studied by Gerts (1999), however the assumption that the contribution will remain constant for the wide FOV is a bold one.

4.6 Secondary Peak

The collected spectra have been measured over the energy range from 0keV to over 500keV as opposed to the previous work, which only measured from 55 to 90keV. The collection of this data resulted in the discovery of a spectral feature, which has not been previously observed.

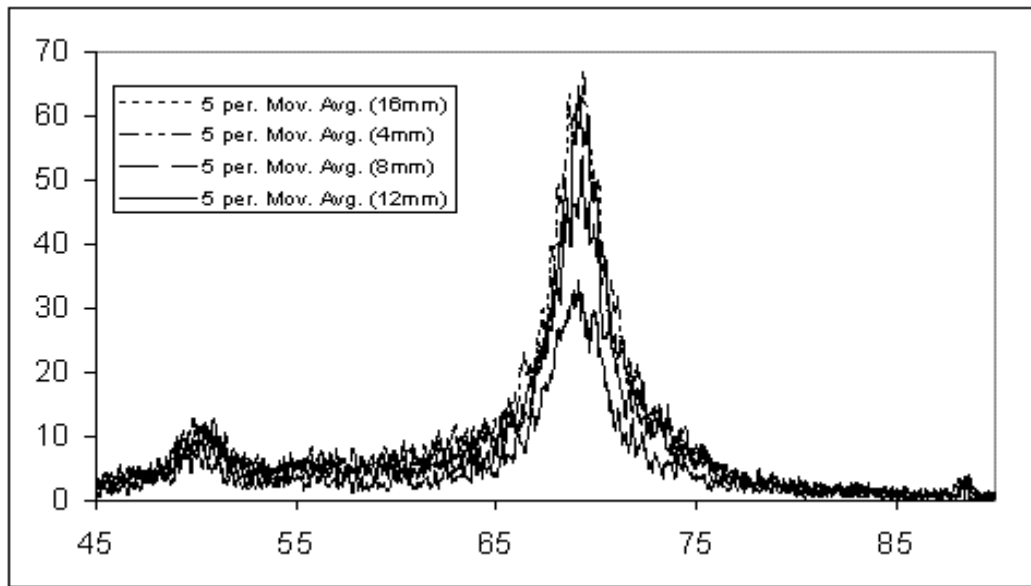


Figure 39: Counts vs. energy (keV), four spectra measured by detector 6, resulting from 4, 8, 12, and 16mm thick samples of Al placed in front of the detector array

The spectra shown are a floating average over seven of the points measured by detector 6. There are 4 spectra each belonging to the 4mm-16mm sample. The 88keV signal may be observed and is the result of photons, which have not interacted with any portion of the MCST system until detection or they are the result of Raleigh scattered events. The largest feature is the singly scattered events and is peaked at approximately 69keV for detector 6. These peaks are expected and are the events modeled by the system and used during image reconstruction. The unexpected signal is that peaking at approximately 52keV. This signal exhibits the same variation in total counts under the peak, as does the singly scattered contribution.

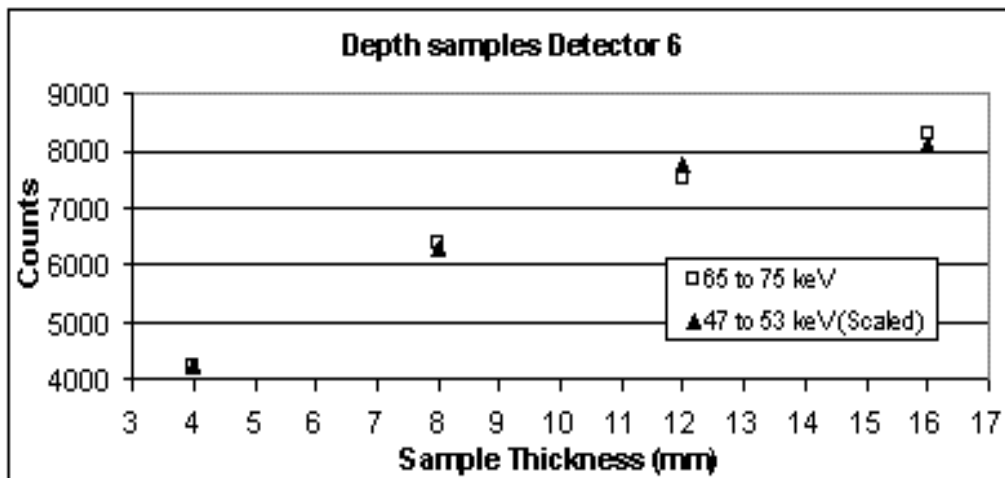


Figure 40: Counts under peaks showing same proportions from singly scattered peak and the secondary peak, the secondary peak is scaled by a factor of 6 to make the relationship apparent

Figure 40 shows the total counts under the single scattered peak (65keV to 75keV) and for the secondary peak (47keV to 53keV). Both peaks appear to exhibit the same intensity as a function sample depth, implying that the secondary peak has a direct relationship with singly scattered photons. The intensity measurements of the secondary peak are scaled by a factor of six to make the relationship between these two sets of measurements more apparent. The factor of six relationship between the intensity of the singly scattered peak and the secondary peak is consistent in all detectors and samples explored. The secondary peak translates along the energy axes as a function of position; however, the relationship is different from that attained for the singly scattered peak

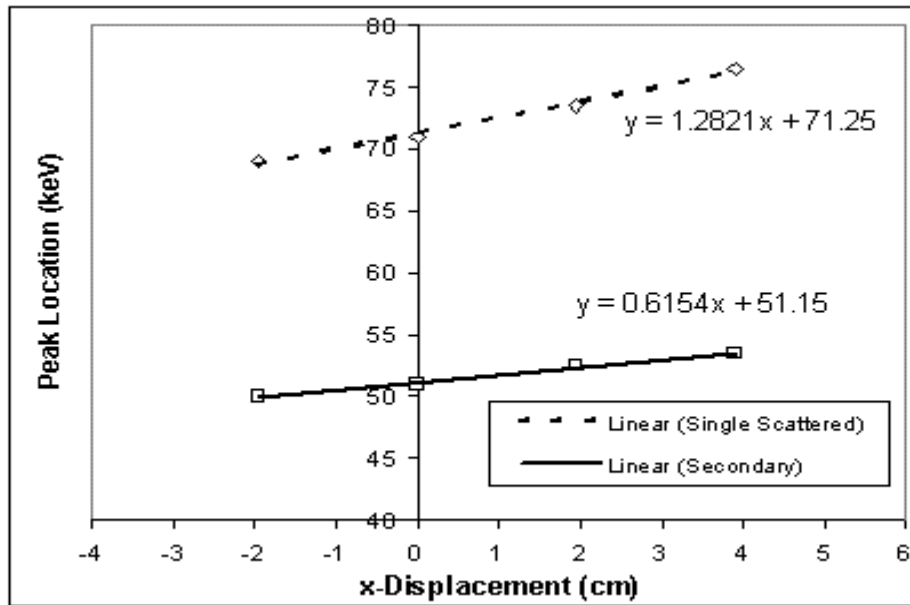


Figure 41: Peak location as a function of the x position of the detectors

From the slope of the lines it is observed that the peak location of the singly scattered peak moves 1.28keV per cm displacement while the secondary peak migrates at 0.62keV per cm. This difference as a function of angle shows that the peak has an indirect relationship with the singly scattered return. The two arguments presented motivate different relationships between the features leaving the cause of the secondary feature undetermined.

Chapter 5: Conclusions

5.1 Summary and Conclusions

The feasibility of multiplexed tomography, using Compton scattered events, has been reaffirmed. Previous efforts have been successful in reconstructing purely aluminum samples. The extension of the program to include material with higher atomic number is a large step in applying this method to real world applications.

Previously the smoothing term included in PWLS caused the electron density of the samples to be spread into the surrounding air. Allowing this to occur caused an overall reduction in the electron densities throughout the samples. By determining the boundaries of the sample, the smoothing is restricted to the area where the material is truly present, increasing the reconstructed electron densities through the sample. The inclusion of discretization forces the voxel densities to have values that are exact for the materials present in the sample. The inclusion of boundary conditions and discretization have reduced the artifacts previously present in images and attain electron density values equal to materials present in the samples.

As seen in the wide field of view measurements, Scatgram does not accurately predict the spectra of detectors 5 and 4 when the rivet is included in the sample. The spectra of these detectors are influenced more by the presence

of the rivet because the path a photon must travel to reach these detectors often encounter the rivet whereas the paths to detector 6 do not. It has been observed that raising the cross-section of iron in the code results in a more accurate prediction of the measurements. This discovery implies that the cross-sections for iron, which was used to approximate steel within the code, differ significantly from the cross-sections of steel. It is suggested that measurements for of the total cross-section of the steel be measured in the lab. Although an exhaustive experimental study of gamma energies would be limited by the sources available in the lab, a relationship could be linearly approximated in the energy range of interest using 88keV and 59.5keV energy peaks. These energies are emitted from ^{109}Cd and ^{241}Am , which are both currently available. Another speculative solution is that the multiple scatter contribution, due to the inclusion of the steel rivet, varies from that of the aluminum samples explored by Gerts (1999). Gerts showed that the multiple scattered contributions have features offset lower in energy from the single scattered contribution. These features were small for aluminum and dependent upon the geometry of the sample. The effect upon multiple scatters, of steel in the sample, is unexplored and if the feature takes on a Gaussian-like form, the measurements will match the simulations. A continuation upon Gerts work is in necessary especially when considering expanding the imaging system to a three-dimensional sampling area.

The experimenter approximates the position of the sample and the source. The uncertainty in these positions translates the peak along the energy axis;

however, it has no effect upon the peak shape. Adjusting the source position input into the code compensates for error associated with these positions. The computer model does not predict spectral intensities well and requires the user determine a scaling term. These steps are viewed as calibration steps and will absorb any user error in the positioning of the sample and the source.

The positioning elements of the predictive code are going to be problem and user dependent; thus, their implementation as calibration steps appears to be appropriate. Therefore, the focus of future work should be the accurate determination of spectral shapes and the diminishing of sampling periods, not the positioning of source and sample.

Over all, the system has proven sufficient for the reconstruction of an aluminum sample including a simulated steel rivet and air. Although, it has yet to be shown that the system is able to differentiate between aluminum and aluminum oxide. The reduction of image artifacts and increased accuracy in electron densities implies the utility of the method and inspires confidence in its future application.

5.2 Recommendations

5.2.1 Experimental

The implementation of a three-dimensional detector array of either high-purity Germanium or cadmium zinc telluride will allow the evaluation of a greater sample area simultaneously. A three-dimensions sampling area will increase detector throughput reducing required sampling periods. The major concern in the implementation of a 3D system is that multiple scattering will overwhelm the useable data. The results for the widened field of view implies the feasibility of implementing a three dimensional system. The remaining hurdle for this method will be the computational time involved in constructed images for a three dimensional space.

The use of a different radioisotope with energy emissions approximately 100keV would be advantages. The 88keV emission from ^{109}Cd makes up only 3.6% of the source emissions requiring the use of active sources for limited useable output. The use of a source emitting in this energy regime with more frequency would allow use of lower activities with higher returns. The use of a radioisotope with, multiple peaks is also feasible in the energy regime with the assumption that the two single scattered contributions may be deconvolved. By doubling the detected signal, one has reduced the required sampling time by a factor of two.

5.2.2 Theoretical

The reconstruction algorithm has proven sufficient for this project and the work of Evans (1999); however, further investigation is warranted to assure convergence of the PWLS algorithm in both a spatial and energetic sense. The solution space for the penalized weighted least squares reconstruction algorithm is not guaranteed to be concave and therefore there is no guarantee that the method will converge to a global minimum. The search for a more appropriate solution space should continue in earnest.

A great deal of effort has been dedicated to the implementation and improvement of the reconstruction algorithm. This effort is primarily due to the poorly conditioned system matrix and the consequences of trying to construct images using that matrix. The difficulty involved in constructing images suggests that perhaps the focus of the problem should not be the determination of an image, but differentiating oxidized samples from pure samples, without the generation of an image. Another contributing factor to discourage the use of the system matrix is that the condition of the system matrix decays as the spatial resolution of the model is increased. Using the spectra directly decreases the importance of the system matrix, increasing the ability of the system to realize higher levels of resolution. With the removal of the necessity for a deterministic code, spectra may be predicted using Monte Carlo techniques adaptable to different geometries. Consideration of this method will also have an effect upon the prediction of the three-dimensional problem. Monte Carlo methods have the ability to provide rough determinations of the solution in a relatively brief period of

time and only need consume significant computational time when a high level of accuracy is needed.

Appendix A

The geometry files supply the FORTRAN code with the dimensions of the sample, the voxel size, source and detector positions and dimensions, definition for the collimator plate, and the sample count and background count periods.

Wide field of view

```
&ProjectTitle
  title = "experimantal rivet one"
/
&PixelData
  minx = -2.3
  maxx = 2.3
  minz = 0.50
  maxz = -0.50
  NX = 46
  NZ = 10
  wd = 0.1
/
&SourceSpecs
  NSrcPos = 6
  dXsrc = 0.5
  dZsrc = 0.5
  NXsrc = 1
  NZsrc = 1
  thetasrc1 = -1.204277
  thetasrc2 = -1.204277
  thetasrc3 = -1.204277
  thetasrc4 = 1.204277
  thetasrc5 = 1.204277
  thetasrc6 = 1.204277
  thetasrc7 = 0.0
  thetasrc8 = 0.0
/
&SourceLocation
  xsrc1 = 8.5
```

```

xsrc2 = 8.5
xsrc3 = 8.5
xsrc4 = -8.5
xsrc5 = -8.5
xsrc6 = -8.5
xsrc7 = 9.0
xsrc8 = 9.0
zsrc1 = 4.500
zsrc2 = 4.500
zsrc3 = 4.500
zsrc4 = 4.500
zsrc5 = 4.500
zsrc6 = 4.500
zsrc7 = 8.0
zsrc8 = 8.0
/
&CollimationS
  NColls = 6
  mcollS1 = -0.61, -0.61, -0.61, 0.61, 0.61, 0.61
  bcollS1 = 2.58, 2.58, 2.58, 2.58, 2.58, 2.58
  mcollS2 = -0.61, -0.61, -0.61, 0.61, 0.61, 0.61
  bcollS2 = 2.00, 2.00, 2.00, 2.00, 2.00, 2.00
  wCollS = 0.254
/
&CollimationD
  NCollD = 0
  mcollD1 = -0.4375 0.0 0.0 0.0
  bcollD1 = 2.1 0.0 0.0 0.0
  mcollD2 = -0.4375 0.0 0.0 0.0
  bcollD2 = 2.3 0.0 0.0 0.0
  wCollD = 0.254
/
&DetectorData
  DeltaXdet = 1.95
  rdet = 0.32
  NArray = 6
  NDet = 1
  theta1 = 0.0
  theta2 = 0.0
  theta3 = 0.0
  theta4 = 0.0
  theta5 = 0.0
  theta6 = 0.0
  theta7 = 0.0

```

```

    theta8 = 0.0
/
&DetectorPosit
    xdet1 = 1.95
    xdet2 = 0.00
    xdet3 = -1.95
    xdet4 = 1.95
    xdet5 = 0.00
    xdet6 = -1.95
    xdet7 = 99990.00
    xdet8 = 99990.00
    zdet1 = 5.30
    zdet2 = 5.30
    zdet3 = 5.30
    zdet4 = 5.30
    zdet5 = 5.30
    zdet6 = 5.30
    zdet7 = 99990.00
    zdet8 = 99990.00
/
&CountTimes
    count1 = 80100.00
    count2 = 69100.00
    count3 = 80100.0000
    count4 = 80100.0000
    count5 = 69100.0000
    count6 = 80100.0000
    count7 = 1.0000
    count8 = 1.0000
/
&BackTimes
    back1 = 80100.00
    back2 = 80100.00
    back3 = 80100.0000
    back4 = 80100.0000
    back5 = 80100.0000
    back6 = 80100.0000
    back7 = 1.0000
    back8 = 1.0000
/

```

Narrow field of view

```
&ProjectTitle
  title = "experimantal rivet one"
/
&PixelData
  minx = -2.3
  maxx = 2.3
  minz = 0.50
  maxz = -0.50
  NX = 46
  NZ = 10
  wd = 0.1
/
&SourceSpecs
  NSrcPos = 6
  dXsrc = 0.5
  dZsrc = 0.5
  NXsrc = 1
  NZsrc = 1
  thetasrc1 = -1.204277
  thetasrc2 = -1.204277
  thetasrc3 = -1.204277
  thetasrc4 = 1.204277
  thetasrc5 = 1.204277
  thetasrc6 = 1.204277
  thetasrc7 = 0.0
  thetasrc8 = 0.0
/
&SourceLocation
  xsrc1 = 8.5
  xsrc2 = 8.5
  xsrc3 = 8.5
  xsrc4 = -8.5
  xsrc5 = -8.5
  xsrc6 = -8.5
  xsrc7 = 9.0
  xsrc8 = 9.0
  zsrc1 = 4.500
  zsrc2 = 4.500
  zsrc3 = 4.500
```



```

zsrc4 = 4.500
zsrc5 = 4.500
zsrc6 = 4.500
zsrc7 = 8.0
zsrc8 = 8.0
/
&CollimationS
  NColls = 6
  mcollS1 = -0.61, -0.61, -0.61, 0.61, 0.61, 0.61
  bcollS1 = 2.58, 2.58, 2.58, 2.58, 2.58, 2.58
  mcollS2 = -0.61, -0.61, -0.61, 0.61, 0.61, 0.61
  bcollS2 = 2.00, 2.00, 2.00, 2.00, 2.00, 2.00
  wCollS = 0.254
/
&CollimationD
  NCollD = 0
  mcollD1 = -0.4375 0.0 0.0 0.0
  bcollD1 = 2.1 0.0 0.0 0.0
  mcollD2 = -0.4375 0.0 0.0 0.0
  bcollD2 = 2.3 0.0 0.0 0.0
  wCollD = 0.254
/
&DetectorData
  DeltaXdet = 1.95
  rdet = 0.32
  NArray = 6
  NDet = 1
  theta1 = 0.0
  theta2 = 0.0
  theta3 = 0.0
  theta4 = 0.0
  theta5 = 0.0
  theta6 = 0.0
  theta7 = 0.0
  theta8 = 0.0
/
&DetectorPosit
  xdet1 = 1.95
  xdet2 = 0.00
  xdet3 = -1.95
  xdet4 = 1.95
  xdet5 = 0.00
  xdet6 = -1.95
  xdet7 = 99990.00

```

```

xdet8 = 99990.00
zdet1 = 5.30
zdet2 = 5.30
zdet3 = 5.30
zdet4 = 5.30
zdet5 = 5.30
zdet6 = 5.30
zdet7 = 99990.00
zdet8 = 99990.00
/
&CountTimes
count1 = 90100.00
count2 = 80100.00
count3 = 75100.0000
count4 = 75100.0000
count5 = 80100.0000
count6 = 90100.0000
count7 = 1.0000
count8 = 1.0000
/
&BackTimes
back1 = 80100.00
back2 = 80100.00
back3 = 80100.0000
back4 = 80100.0000
back5 = 80100.0000
back6 = 80100.0000
back7 = 1.0000
back8 = 1.0000
/

```

Wide collimation settings

```

1
0.75 0.53125
-2.00 1.00
0.75 0.53125
-2.0 1.00
0.75 0.53125

```

-2.0 1.00
-0.75 -0.53125
-2.0 1.00
-0.75 -0.53125
-2.0 1.00
-0.75 -0.53125
-2.0 1.00

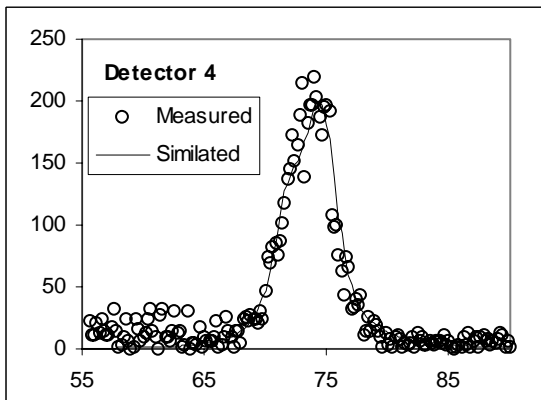
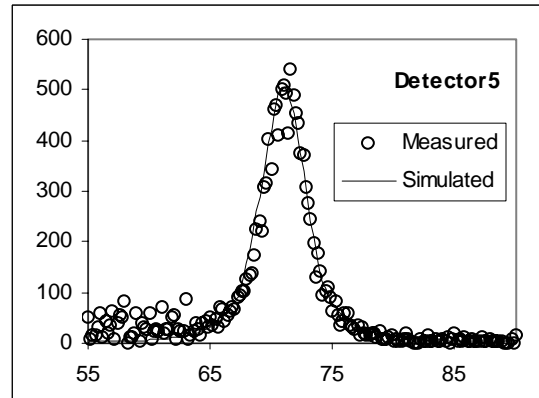
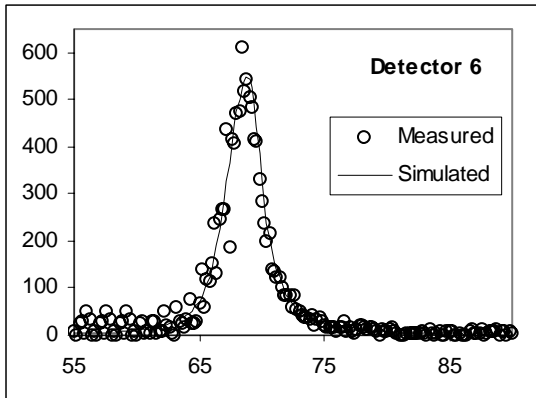
Narrow collimation settings

1
0.75 0.53125
-1.00 0.70
0.75 0.53125
-1.00 0.70
0.75 0.53125
-1.0 0.70
-0.75 -0.53125
-1.0 0.70
-0.75 -0.53125
-1.0 0.70
-0.75 -0.53125
-1.0 0.70

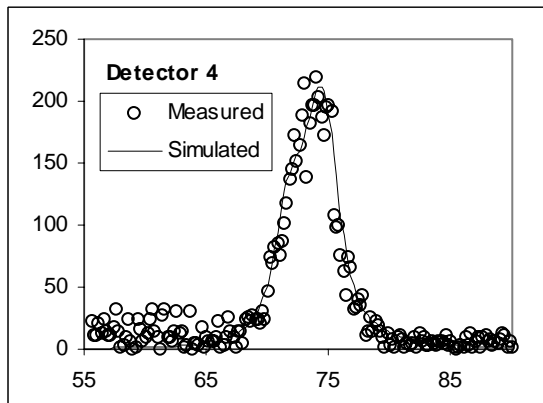
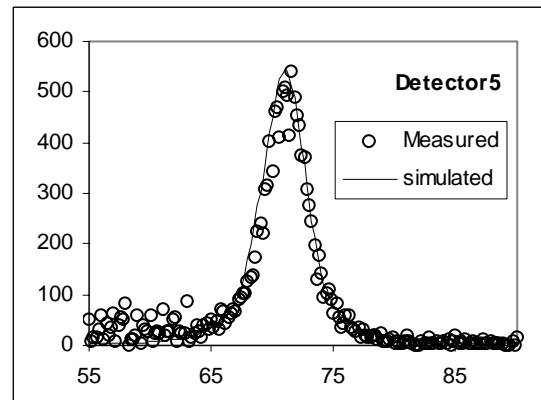
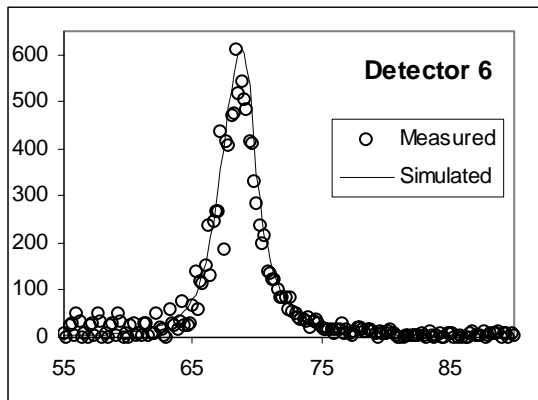
Appendix B

Spectra comparison of measured to simulated data for the geometries not already included in the text. Only detectors 6, 5, and 4 are shown because 1, 2, and 3 may be derived from them.

Inclusion of top boundary



Inclusion of top an bottom boundaries



References

- Biggs, F., L.B. Mendelsohn and J.B. Mann. "Hartree-Fock Compton Profiles," Atomic Data and Nuclear Data Tables, Vol. 16, No. 3: 202-222 (September 1975).
- Costescue, Cornel. To be published.
- Cooper, Malcom J., "Compton Scattering and the Study of Electron Momentum Distributions," Radiation Physics and Chemistry, Vol. 50, No. 1: 63-75 (July 1997).
- Fessler, Jeffrey A. "Penalized Weighted Least-Squares Image Reconstruction for Positron Emission Tomography," IEEE Transactions on Medical Imaging, Vol. 13, No. 2: 290-300 (June 1994).
- Gerts, David. Double Scatter Spectrum for the Multiplexed Compton Scatter Tomograph. MS thesis, AFIT/GAP/ENP/99M-03. Graduate School of Engineering, Air Force Institute of Technology (AU), Wright-Patterson AFB, OH, January 1999.
- Knoll, Glenn F. Radiation Detection and Measurement, New York: Wiley, 1989.
- Kondic, N., A. Jacobs and D. Ebert. "Three-Dimensional Density Field Determination By External Stationary Detectors and Gamma Sources Using Selective Scattering," Proceedings of the Second International Topical Meeting on Nuclear Reactor Thermal-Hydraulics: 1443 - 1455 (January 1983).
- Ribberfors, R., K.-F. Berggren. "Incoherent-X-Ray-Scattering Functions and Cross Sections $(d\sigma/d\Omega')_{incoh}$ by Means of a Pocket Calculator," Physical Review A. Vol. 26, No. 6, 3325-3333, (December 1982).
- Sauer, Ken and Charles Bouman. "A Local Update Strategy for Image Reconstruction from Projections," IEEE Transactions on Signal Processing, Vol. 41, No. 2: 534-548 (February 1993).

Zhu, P., P. Duvauchelle, G. peix, D. Babot, "X-ray Compton backscattering techniques for processing tomography: imaging and characterization of materials." IOP Publishing Ltd. (1996).

Vita

Matthew A. Lange attended North Canton Hoover High School. Upon graduation he began his college career at Grove City College in Pennsylvania. After two years at Grove City College Matt returned to his hometown and continued his academic quest at the University of Akron. It was there that he developed a zeal for physics and decided to continue his education. His bachelor's degree in physics completed, Matt traveled to Dayton, OH, to attend the Air Force institute of technology. Under the guidance of this prestigious establishment, dedicated to the development of minds, this document has been formed. Have a nice day!